THE PENNSYLVANIA STATE UNIVERSITY
SCHREYER HONORS COLLEGE

DEPARTMENT OF MATERIALS SCIENCE AND ENGINEERING

Novel Processing Strategies for Laser Powder Bed Fusion to Reduce Defects in High Temperature TZM Alloy

JAMES HANAGAN
SPRING 2022

A thesis
submitted in partial fulfillment
of the requirements
for a baccalaureate degree
in Materials Science and Engineering
with honors in Materials Science and Engineering

Reviewed and approved* by the following:

Edward W. Reutzel
Associate Research Professor
Thesis Supervisor

R. Allen Kimel
Associate Teaching Professor
Honors Adviser

* Electronic approvals are on file.

ABSTRACT

TZM is a high temperature molybdenum alloy that is of interest for aerospace, nuclear power, and medicine, and additive manufacturing (AM) offers the ability to generate novel designs for these applications, but there is little in the literature that investigates AM of TZM. In this work, the ability of TZM to be processed via laser powder bed fusion (LPBF) is investigated. Novel laser processing parameters, including double exposure of every layer and shorter hatch lengths, are utilized to influence melt pool morphology and solidification in attempting to create a defect free microstructure without the need to heat the build substrate to extreme temperatures. For each type of process strategy used, a variety of combinations for laser power, scan speed, and hatch spacing are tested. In addition, a novel specimen geometry is utilized to test the limits of TZM for processing fine features and support structures. With this set of laser parameters, relative densities as high as 99.76% and microhardness values as high as 400 HV are achieved. It is determined that the double exposure processing strategy is not shown to be effective as a method of processing TZM due to high defect quantities in the microstructure and high rate of build failures (e.g. due to cracking and distortion) among those specimens. Short hatch lengths, on the other hand, prove to be quite effective with 100% of specimens using a laser scan speed of 600 mm/s being built successfully to completion. These specimens had similar microstructures to the normal exposure specimens, so as a result it appears that hatch lengths anywhere from 0.5 mm to 5 mm showed potential for further optimization. Ultimately, this work shows that LPBF of TZM without high build substrate heating holds promise for producing TZM structures with minimal defects and limited cracking.

TABLE OF CONTENTS

LIST OF FIGURES

LIST OF TABLES

ACKNOWLEDGEMENTS

Financial support for this project was provided by internal Penn State Applied Research Lab funding. I would like to thank all students, faculty and staff at CIMP-3D who helped me along the way in completing this research. Special thanks go to Jack Jenny, Zack Snow, Scott Tokarz, Ken Meinert, and Ryan Overdorff for their generous time given to assisting me with everything from instrument training and AM processing to literature searches and sample preparation. I'd also like to thank Jayme Kiest, Abdalla Nassar, and Doug Wolfe for their helpful expertise and input given to me throughout the process of this research. All TZM powder feedstock was generously donated by H.C. Starck, along with invaluable expertise given by Scott Ohm and Faith Oehlerking. Lastly, but most certainly not least, I would like to express my deepest gratitude to Ted Reutzel for his constant support, patience, and guidance throughout this project as my advisor. Without all this help, none of this research would have been possible.

Chapter 1

Introduction

Background

Additive manufacturing (AM) is a general term applied to any process where material is deposited in a layer-by-layer fashion to build a near net shape part. In this investigation, laser powder bed fusion (LPBF) is the AM technique used. In this technique, metal powder is spread from a reservoir layer-wise over a build substrate usually with a roller or blade. A portion of each layer is then scanned with a laser which melts and solidifies that layer to previous ones. After each layer the build substrate moves down, and another layer is deposited. The resulting part is removed from a bed of unsolidified powder and cut from the build substrate. From there, post-process steps such as heat treatment may be taken. AM is a beneficial processing technique for both prototyping and end-use parts as it can be used to create complex geometries for little extra cost, and it excels at producing one-off or low volumes of parts relatively quickly and cost-effectively compared to traditional processing techniques. For this reason, it is beneficial to be able to have this processing technique available when manufacturing a part using any material system.

According to current literature, however, refractory metals such as tungsten and molybdenum have yet to be successfully processed to high density free of cracking using AM without the use of highly specialized equipment. Tungsten and molybdenum are known for having extremely high ductile-to-brittle transition temperatures (DBTT) hundreds of degrees above room temperature. Because of this, AM processes like LPBF that require repeated,

localized heating and cooling of the part build up residual stresses that tend to lead to microcracking as the part cools. One remedy that has been used in literature is to preheat the build substrate well above the DBTT, thus reducing thermal gradients and residual stresses while also avoiding a brittle microstructure which exacerbates microcracking. While this technique has been successful in reducing cracking, it is not always practical as it requires heating the build substrate up to as high as 1000 °C and does not completely eliminate cracking [1]. Typical AM machines are not capable of heating to this high of a temperature without significant re-engineering. For this reason, it is worthwhile to search for another method of reducing cracking that does not require such specialized equipment.

TZM is a common Mo alloy which contains 0.5 wt.% titanium, 0.08 wt.% zirconium, and carbon which tends to vary in concentration. It is known for its high temperature strength and creep resistance compared to pure Mo due to particle strengthening and higher recrystallization temperature. TZM has been found to react with oxygen present in the environment during AM, producing ZrO_2 precipitates within grains rather than MoO_2 precipitates at grain boundaries as seen with pure Mo [2]. This increases grain boundary strength, thus reducing intergranular cracking commonly seen in pure Mo. As such, adding alloy elements to help prevent oxygen from migrating to grain boundaries is another potential remedy for cracking in molybdenum.

The ability to successfully process TZM using AM would have significant implications in the alloy's primary applications in aerospace, nuclear power, and medicine. AM would enable more sophisticated design of lightweight, complex, high temperature components such as rocket nozzles. Additionally, it would allow for reduced quantity of parts in all applications by combining assemblies into single, continuous parts. To this end, more investigation into processing TZM would be beneficial to determine how printable this alloy is.

Objective

This investigation seeks to determine the processability of TZM via LPBF under a wide range of process conditions by assessing build quality through a number of criteria. First, it will determine whether TZM can be processed to more than 99.0% relative density by any of a collection of selected laser parameter sets. It also will investigate whether laser parameters such as novel scan strategies can be used to reduce cracking within the alloy by influencing the melt pool morphology and solidification behavior. Additionally, the ability to create fine features with TZM will be examined by producing specimens of a unique design not used in previous investigations of TZM. Finally, the viability of TZM processed using AM must be established by comparing properties such as hardness to those of traditionally processed TZM.

Considerations in Engineering and Design

Economic considerations were made in a number of different aspects of this investigation. Firstly, cost of materials was considered in the selection of a high temperature material for the stated applications to develop LPBF processing parameters. The material was narrowed down to TZM partially because of its reduced cost compared to similar refractory alloys. From communication with H.C. Starck, it was estimated that purchasing the necessary 10 Kg quantity of C103 niobium powder would cost from $1,200/Kg to $1,500/Kg, while 20 Kg of Ta-10W tantalum-tungsten powder would cost $1,200/Kg. By comparison, the 20 Kg of TZM powder used for this investigation were estimated at $350/Kg. Although this powder was generously donated free of charge by H.C. Starck, these costs are certainly still worth considering not only for further investigations but also for applications using this material in the

future. Retooling costs were considered in this work as a motivation to develop the LPBF process for TZM. LPBF is known to reduce costs associated with retooling any time a design is altered for a part because the only necessary step for this change to take place is preparing and uploading new build files to the system. For traditional manufacturing methods, retooling involves design and manufacturing of new molds, fixtures, and workflows which adds cost.

Arguably the largest consideration made in this project, manufacturability is the focus of the problems this investigation set out to solve. This work seeks to advance the manufacturability of TZM to the point that no highly specialized, expensive equipment is required to process TZM without defects using LPBF. If successful, the techniques used in this paper should widen the field of LPBF machines capable of processing TZM without defects.

Finally, sustainability was considered for this work. TZM is a well-established refractory alloy with numerous applications. It has been used for many decades and it will likely continue to be used in coming decades. For these reasons, it would be beneficial to expand the catalogue of processing techniques available for use with TZM. LPBF in particular would open up new possibilities in making parts lighter, reducing material costs, and allowing for more rapid design and manufacturing of low quantities of parts. This would only serve to increase demand for this important material in the future, making this a highly sustainable project.

Chapter 2

Literature Survey

This investigation focuses on the processing of TZM molybdenum powder by laser powder bed fusion (LPBF), thus it is beneficial first to examine past work done on LPBF of TZM. Since there is little published on LPBF of TZM, research was expanded to LPBF of Mo and its alloys. In order to determine how TZM specifically behaves during melting and solidification, the search was broadened further to welding, as this subject can provide insights on how TZM behaves when subjected to a highly concentrated source of heat. Additionally, as this investigation also addresses post-build treatments of TZM to achieve desired density, it is worthwhile to investigate work related to the behavior of TZM subjected to hot isostatic pressing (HIP) or stress relief. Finally, a major challenge observed in LPBF of Mo and its alloys is cracking and porosity. As such, the causes and potential remedies of cracking and defects in additively manufactured parts will be addressed.

Laser Powder Bed Fusion of Molybdenum and its Alloys

Pure Mo has proven to be a challenging material to process with LPBF. For example, J. Braun et al. found that a network of intergranular cracks tends to form during the processing of pure Mo [1]. They note that this is caused, in large part, by the segregation of oxygen to grain boundaries in the form of MoO_2 during solidification. As a result, the ductile-to-brittle transition temperature (DBTT) of the Mo is raised above the substrate temperature while processing, and cracks freely propagate under the accumulation of residual stresses common in LPBF. They suggest that cracking could be reduced by greatly reducing oxygen concentration in the build

chamber and heating the build plate above the DBTT to 1000 °C, but even with these conditions—difficult to produce without highly sophisticated equipment—they were unable to completely eliminate cracking. M. Higahsi and T. Ozaki found that while pure Mo can be processed to a low degree of porosity with sufficiently high volumetric energy densities, electron backscatter diffraction measurements revealed a high degree of texturing in the microstructure [3]. It was also found that crystallographic texturing changed from strong texturing in the <110> direction at high laser power and low scan speeds to strong <001> texturing at low laser power and high scan speed. Of the defects that were found, both lack of fusion and keyhole porosity were most common. D. Faidel et al. also found that sufficiently high energy input is required to achieve high densification in pure Mo due to its high melting point. With a relatively low laser power of 200 W, the highest relative density they were able to produce, measured with optical techniques, was 82.5% [4]. This density was achieved using a 200 W laser, 556 mm/s scan speed, 25 µm layer thickness, and 30 µm hatch spacing, which represents an intermediate volumetric energy density tested in the study. Volumetric energy density appears often in discussion of LPBF, so it is important to define this parameter. Equation 1 defines the simple mathematical relationship between laser parameters and volumetric energy density.

$$Volumetric\ energy\ density = \frac{P}{hvt} \tag{1}$$

Volumetric energy density is typically defined as the power of the laser, P, divided by the hatch spacing between laser scans, h, the velocity of the laser, v, and the thickness of the powder layer, t. Though not always an ideal metric to correlate with material density, it can occasionally provide insight into the total amount of energy put into a part over the course of processing. It can also help to identify the cause of certain defects like lack of fusion porosity and deformation

from residual stresses. In the case of LPBF of Mo, it is likely that higher laser power than the 200 W used by Faidel et al. is necessary to achieve higher densification.

In other work with pure Mo, D. Wang et al. were able to successfully process Mo to as high as 99.1% density with no cracking by printing parts on a low-density support structure and rotating laser scans by 67° between layers [5]. The idea behind the support structure is that it reduced conductive heat loss to the build substrate, reducing residual stresses from thermal gradients in the part and keeping the part at a higher temperature. The 67° rotation between layers creates irregularly shaped grains in the build direction, presumably helping to resist cracking along grain boundaries. Though the results from this investigation are promising, it remains to be seen whether the strategy of building a low-density support structure under all parts is a viable method for larger parts or those with more complex geometry. These design/build strategies can occasionally result in delamination of the part from the build substrate. So, with a support structure, such distortion is more likely to occur, leading to a failed build.

To summarize, the primary challenges faced when processing pure Mo via LPBF are microcracking, thought to be caused by oxides weakening grain boundaries and residual stress, and porosity, likely caused by suboptimal laser parameters. Potential remedies for these problems have been explored, typically in the form of keeping the part at an elevated temperature by either heating the build plate to an extremely high temperature or building parts on top of a thermally insulative support structure. The issue with these methods of defect mitigation is that they either require highly specialized equipment (in the case of heating the build plate to extremely high temperatures, which cannot be done with the stock build plate heating feature in most LPBF machines), or they may not be applicable to all parts (in the case of the insulative

support structure). For these reasons, alloying Mo may be a more favorable approach to building defect free parts.

Since pure Mo poses many challenges in LPBF that cannot be solved, changing the composition of the material been proposed as a method of reducing defects in the processing of this refractory metal. Carbon has been studied as one potential element to alloy with Mo for defect-free processing. For example, L. Kaserer et al. alloyed Mo with about 0.45 wt.% C and found that this altered the fracture mode from the intergranular mode often observed in pure Mo to a transgranular mode [6]. With this alloy, 99.7% dense parts with no cracking were built, and alloyed samples increased bend strength and hardness by 340% and 65%, respectively compared to pure Mo. These results were corroborated when J. Braun et al. also found that alloying Mo with C at a concentration of about 0.45 wt.% can entirely eliminate cracking and result in 99.5% dense samples [7]. This was determined to result from the fact that the alloy forms Mo_2C precipitates that trap the majority of the oxygen and keep it from segregating to the grain boundaries in the form of Mo oxides. As a result, grain boundary strength is improved and cracking along grain boundaries is prevented. Finally, L. Kaserer et al. also investigated LPBF of Ti-Zr-C-Mo alloy TZM and discovered that in this alloy oxygen is not only bound in Mo and Mo-Ti carbides, but it also forms ZrO_2 within grains as well [2]. Because of this, a similar result was found in that the fracture mode was transgranular and no oxygen was able to be found on grain boundaries in samples that were processed to as high as 99.7% density.

Welding of TZM

Since prior work in LPBF of TZM is limited, some investigation into welding of TZM may be beneficial to better understand how this alloy behaves when subjected to a highly concentrated, high power heat source such as a laser or electron beam. J. Wadsworth et al. experimented with welding TZM butt joints using electron beam welding (EBW), laser welding (LW), and even tungsten inert gas (TIG) welding [8]. EBW was done at 120 kV, beam current of 16 mA, and a vacuum of 0.27 mPa. TIG was done with a pulsed current of 240-100 A and a voltage of 20V, inside of a chamber with 66% He and 34% Ar by volume. LW was done with a 10 kW CO_2 laser within an Ar atmosphere. All welds were found to be defect free with the exception of some very small (<10 μm) pores in certain TIG welded samples. Despite this, all samples tested for tensile strength failed in a brittle mode. This was thought to be caused by the significantly coarser grains found in the weld compared to the base metal of the joint. As a result, the weld took the majority of the strain, and therefore strain rate, when under stress. When a lower strain rate was used for testing, samples tended to fail in more ductile modes.

J. Ning et al. tried welding TZM lap joints with a 1000 W ytterbium fiber laser, and the main challenges they faced were cracking and porosity in addition to embrittlement [9]. Out of a number of conditions which were varied, adding a gap between the two pieces of base metal in the joint appeared to have the greatest effect on reducing porosity in the weld. They suggested this is likely because the gap allowed for an additional path for keyhole porosity to escape from the weld prior to solidification. Other conditions tested included heat input rate, which was found to increase porosity. To assess influence of heat input rate, welds at 850 W laser power were tested at two different speeds: the lower heat input speed being 1.0 m/min, and the higher heat input speed being 0.5 m/min. Of the two conditions, the higher speed, lower heat input case

resulted in more than 3 times less porosity by volume compared to the higher heat input case. Also, the pores found in the latter case tended to be much larger in diameter than those in the former. This effect of travel speed on porosity is important to keep in mind as laser parameter experiments are carried out in LPBF.

The effect of heat input on fiber laser welded Mo was also investigated by M. Xie et al., who welded a material designated as nanostructured high-strength molybdenum alloy (NS-Mo), which is a Mo substrate with 0.5 wt% of dispersed nano-sized La_2O_3 particles [10]. While welding socket joints with varying heat inputs, they also found that increasing heat input tended to increase porosity. The porosity in high heat input samples had an irregular morphology thought to be caused by keyhole instability, while low heat input samples had spherical pores thought to be caused by existing porosity in the base metal produced via powder metallurgy. This knowledge may be transferrable to LPBF of TZM because any porosity produced in prior layers will likely not have time to escape when that material is partially remelted during later layers. Additionally, any exceedingly high heat inputs in LPBF will create similar porosity caused by an unstable keyhole.

In their technical report on TIG welding of TZM, G. Hanks also recommended using base metal with as little porosity as possible, which was found to be arc-cast TZM sheet [11]. In addition to base metal choice, a recommendation was also made for stress relieving welds directly after welding at about 900 °C for 1 hr. This is to avoid initiating and propagating microcracks after welding. Also, welding speed must remain constant and not too fast or slow to ensure that porosity and residual stresses are minimized. To achieve this, it was recommended that welding be done using automatic equipment to achieve constant weld speeds and avoid building of residual stresses.

Finally, S.P. Chakraborty and N. Krishnamurthy also investigated electron beam welding of TZM, and they successfully created defect-free welds [12]. To avoid cracking, the base metal was preheated to above the DBTT, and each weld was stress relieved at 1000 °C for 2 hrs under high vacuum afterward. Another potential reason contributing to defect-free welding is that all processing was done in a vacuum of about 10^{-5} torr. This leaves little potential for contamination and embrittlement of welds by oxygen, but also helps to remove gas that may lead to porosity in the weld. This leaves the most likely cause of porosity to be by vaporization of constituents within the alloy itself. This, however, was shown to not be a serious issue in this experiment as x-ray fluorescence (XRF) analysis showed only a marginal decrease in Zr and Ti content in the weld – 0.02 wt.% and 0.03 wt.%, respectively. Hardness measurements showed that the hardness gradually decreased from the base metal approaching the center of the weld. This is likely due to the substantial increase in grain size from the rolled TZM sheet base material to fusion zone of the weld. Several combinations of welding parameters were used, however a concrete comparison between these combinations was not made, therefore they were unable to draw any conclusions about heat input and weld quality.

Post-processing of TZM

As was mentioned in the discussion of welding Mo alloys, post-processing stress relief can be a viable method of reducing cracking in TZM [11,12]. For this reason, a search through literature to find common stress relief temperatures for TZM is beneficial. As seen already in work by G. Hanks, and S.P. Chakraborty and N. Krishnamurthy, TZM welds can be successfully stress relieved by heating at either 900 °C for 1 hr [11], or by heating at 1000 °C for 2 hr in a

vacuum [12]. To examine the microstructure and tensile strength of forged TZM, J. Warren and G. Reznikov used material that was stress-relieved at 1550 °C for 30 minutes [13]. They also mentioned that 1100-1200 °C is a typical temperature at which to stress relieve TZM. It is not immediately clear why they decided to go with the higher temperature. That being said, the stress-relieved tensile samples appeared to fail in a predominantly ductile fashion, so cracking must not have been extensive, and the stress relief may have had the desired results. In their investigation of the mechanical properties of TZM, B. Cockeram et al. stress relieved their arc-cast, wrought TZM at 1150 °C for 30 minutes in a vacuum furnace [14]. Any cracking which occurred appeared to have originated during tensile testing as opposed to residual stresses, so this stress relief appears to be successful. In other work, TZM sheet was stress relieved at about 930 °C for 15 minutes by K Abe et al., which appeared to not lead to any negative effects in properties associated with residual stresses [15].

Another potential post-processing technique that could be used for LPBF TZM is HIP. This technique is being considered as it has been shown to heal microcracks in similar metals such as tungsten after LPBF [16]. J. Barranco et al. tested HIP with a number of different TZM specimens, with temperatures ranging from 1400 to 1600 °C, pressures of 15 to 30 ksi (1034 to 2068 bar), and times from 1.5 to 3 hours [17]. TZM specimens processed with HIP included spherical powders with average particle sizes ranging from 24.7 to 220 μm, pressed and sintered TZM bar, and arc-cast wrought bar. Within these ranges, no single set of parameters appeared to stick out as the most beneficial because there was too much variability in mechanical property results. However, most samples using these parameters were successfully densified to 10.0-10.1 g/cm^3 which is very close to TZM's theoretical density of 10.2 g/cm^3. As a result, it appears that any of these HIP recipes could be successful if used on LPBF TZM. In other work, S. Majumdar

and I.G. Sharma experimented with a number of powder consolidation and sintering techniques with TZM [18]. One of these techniques involved cold isostatic pressing (CIP) TZM to initially compact the powder, pre-sintering at 950 °C for 2 hours under hydrogen flow, then HIPing at 350 bar (5 ksi) and 1250 °C for 4 hours. A density of 10.16 g/cm^3 was achieved using this technique, though it is difficult to explain how such a low temperature and pressure was successful for HIPing. It could be because of the CIP or pre-sintering steps mostly densifying the part prior to HIP, or because it was done at a relatively longer time of 4 hours.

Common Defects in Additive Manufacturing

There are a number of defects commonly observed in additively manufactured metals, and it is useful to know what causes them and how to mitigate their formation in parts. With this knowledge, analysis of defects in prior builds can be used to diagnose and rectify issues with processing parameters, allowing for defect-free parts to be built. In fusion-based processes like LPBF, typical types of porosity seen are lack of fusion, keyhole collapse, and gas-entrapment [19]. Lack of fusion porosity, as the name suggests, is a lack of complete fusion of the powder bed that appears as elongated, irregularly shaped pores of anywhere from 50 μm to more than 1 mm in size which often contain unmelted powder particles. These shapes of defects can severely degrade mechanical properties as their sharp corners can concentrate stresses and initiate cracks easily. This porosity is often caused by less-than-optimal laser parameters such as hatch spacing (the distance between subsequent scan lines) being too large. Other parameters affecting the formation of this type of porosity include laser travel speed, spot size, and power. If there is insufficient overlap between laser passes on the powder bed, lack of fusion porosity is highly

likely to develop. Keyhole collapse porosity is a type of porosity typically associated with high laser energy densities. It is caused by a deep melt pool which becomes unstable and ejects material, leaving behind pores in the melt pool as it solidifies. Keyhole pores can vary in size and shape, but they are typically between 10 μm and 50 μm in size. Gas porosity can be caused by a few different factors, such as gas entrapment, supersaturation of gases dissolving in the melt pool, and creation of gases through chemical reactions in the melt pool. They usually have a characteristic spherical shape and range in size from 5 μm to 20 μm.

In addition to porosity, cracking is another type of defect commonly seen in AM, and molybdenum, as previously shown, is no exception to this [1,4–6]. Solidification cracking is a very common type seen in LPBF and can be caused by any number of thermal and metallurgical factors; however, solidification cracking typically requires high thermal strain combined with susceptible microstructure to occur [19]. Metallurgical influences on solidification cracking include solidification range of the alloy, ability to backfill dendrites with molten metal as it solidifies and shrinks, dendrite coherency, eutectic fraction, surface tension, grain structure, and grain boundary strength. Mechanical factors in hot cracking include amounts of stress and strain, strain rate, and amount of restraint present on the solidifying alloy. In Mo alloys, some previously observed reasons for cracking include reduction in grain boundary strength from diffusion of oxides, temperatures repeatedly cycling from above the DBTT to below it, combined with significant thermal gradients and stresses already observed in the LPBF process [1,4–6]. Recently, an effort has been made by B. Mondal et al. to computationally determine cracking susceptibility using physics informed machine learning [20]. The factors they used to determine cracking susceptibility included temperature gradient present in the melt pool, solidification growth rate, solidification stress, and ratio of the relaxation time (where the melt

pool is in the early stages of solidification and cracking is not likely) to the vulnerable time (where the melt pool is vulnerable to cracking in the later stages of solidification). Ultimately, it was found that solidification stress had the most influence on cracking susceptibility, while the cooling rate (temperature gradient multiplied by solidification growth rate) had the least influence on cracking susceptibility of the factors considered. As a result, minimizing solidification stress seems to be the most effective way to reduce cracking in AM.

Chapter 3

Experimental Procedure

The TZM powder used in this investigation was provided by H.C. Starck Inc. The composition and particle size distribution of the powder are provided in table 1 and table 2, respectively. This powder was produced using a process which first involved spray drying, followed by sintering and then plasma spheroidization. Figure 1 shows an SEM image of the powder provided by Scott Ohm of H.C. Starck.

Table 1: Composition of the TZM powder.

Element	Mo	Ti	Zr	C	O	Fe	Ni	Si
Concentration (Wt. %)	Balance	0.47	0.08	0.139	0.071	0.0063	0.0161	0.0066

Table 2: Particle Size distribution of the TZM powder.

D10 (µm)	D50 (µm)	D90 (µm)
16.38	28.43	44.89

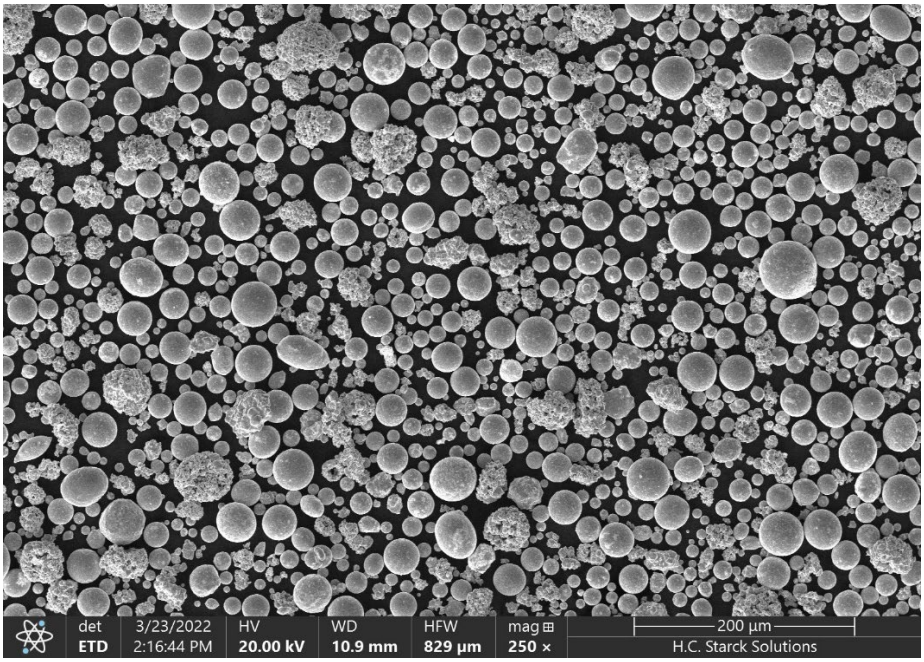

Figure 1: SEM image of the TZM powder.

All TZM samples were built in a 3D Systems ProX 320. Each sample, as shown in figure 2, had a geometry consisting of a sturdy support structure on the bottom to reduce conductive heat loss to the build substrate, a simple block in intermediate layers for examination of bulk microstructure and hardness, and a hexagonal arrangement of pins on the top surface to assess ability to create fine features. All samples were produced during the same build and arranged in a grid on the build substrate. Each sample was built with a layer height of 30 µm, and on each layer the laser scan was rotated by 67° which was shown to produce more irregular grain boundaries in literature to stop cracking [2,5].

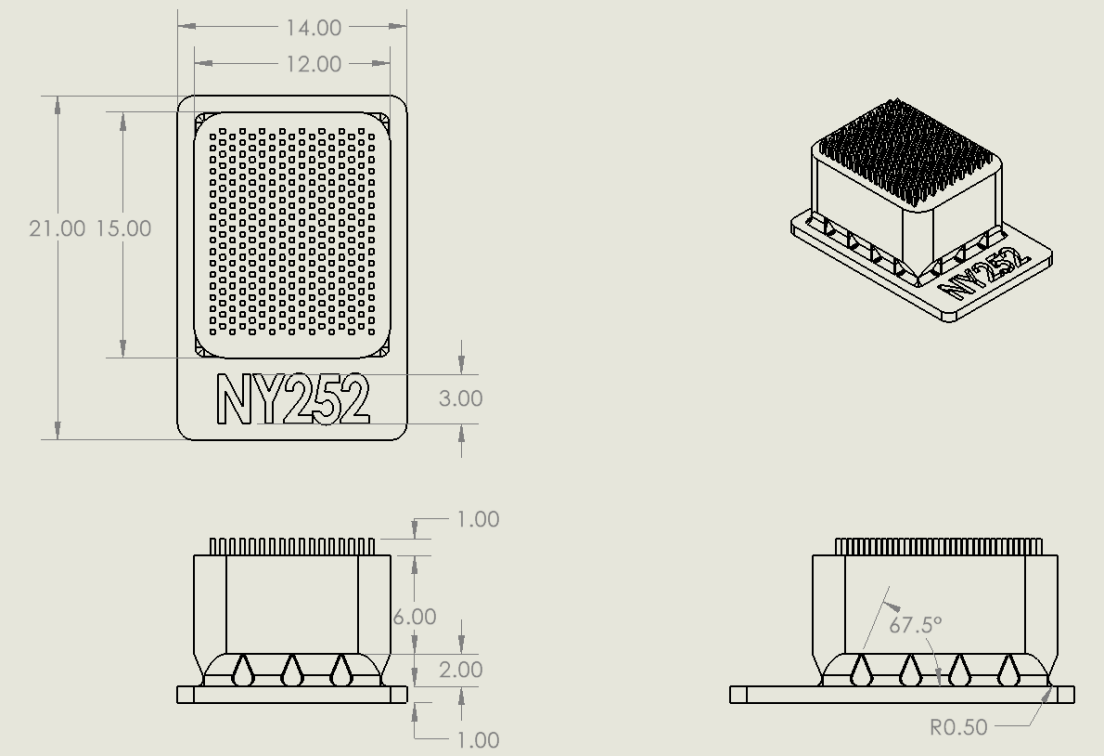

Figure 2: Sample geometry.

The ProX 320 was purged multiple times to achieve the lowest oxygen concentration possible within the build chamber during the build. Figure 3 below shows the oxygen content

present in the build chamber at the start of each layer. The concentration started at 50 ppm on the first layer and decreased until leveling out at about 1 ppm. Then, at layer 186 the build was halted over a weekend so it could be restarted for continued monitoring. This meant that the oxygen concentration increased back up to around 45 ppm before again decreasing down to 1 ppm for the remainder of the build. In future experiments, oxygen should be reduced back to <1 ppm prior to resuming processing after any pauses. Monitoring by an operator was necessary because novel and untested laser parameters were being implemented, and any samples showing signs of failure (e.g. excessive distortion) during the build had to be individually terminated to avoid damaging the recoater, other samples, and the machine. Parameters which were varied between samples included laser power, laser scan speed, hatch spacing, and infill strategy. 2 samples were produced for each set of parameters to have a replicate. A full list of parameter sets for samples are included in Appendix A.

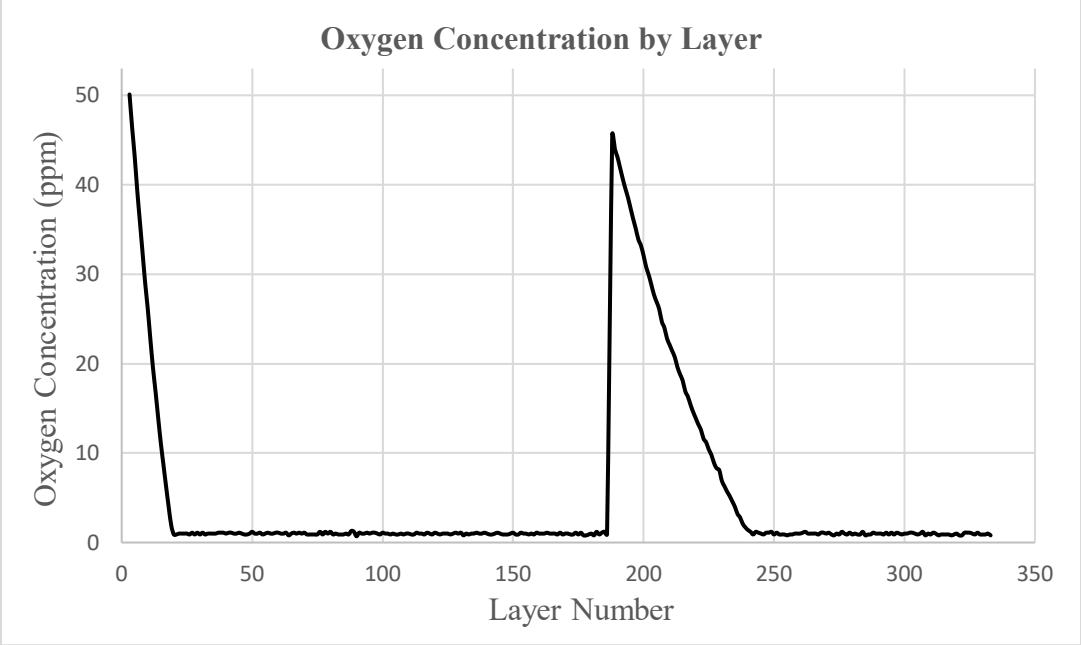

Figure 3: Oxygen concentration in the build chamber for each layer of the LPBF process.

Infill strategies used are illustrated in figure 4. Normal exposure consists of scanning the laser back and forth in stripes that are 5 mm wide across the powder bed. Double exposure is similar to normal exposure except scans are done twice prior to recoating—the first being at a higher laser power and the second being at a lower laser power—before the next layer of powder is deposited. This is being tested because it may keep the part at an elevated temperature in an attempt to avoid cracking from cooling below the DBTT. The short hatch scan strategy involves scanning each layer once as with normal exposure, however the stripes that the laser scans back and forth within are either 1 mm or 0.5 mm in width. This narrower stripe was used to increase the width of the melt pool, therefore effecting solidification dynamics, and possibly affecting cracking susceptibility.

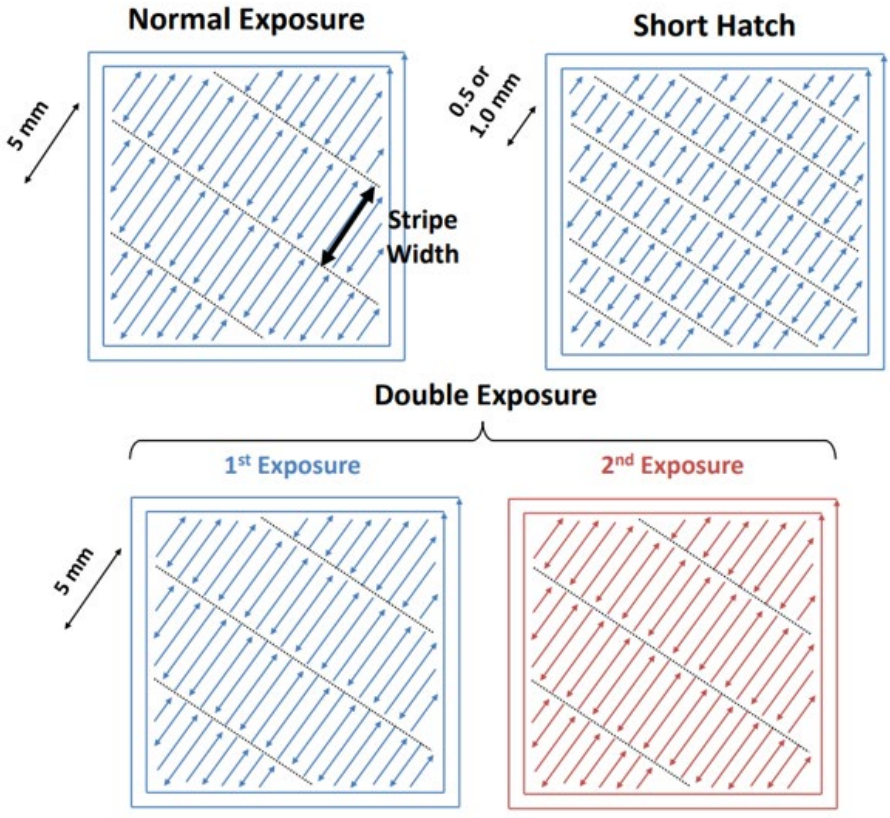

Figure 4: Schematics of each infill strategy.

After the samples were built and cut off the build plate, the density of samples was measured using a Micrometrics Accupyc II 1340 helium pycnometer at the Penn State Materials Characterization Lab. They were then cut with one section being mounted in resin, polished, and etched with Murakami's reagent for microscopy. The other section was cut using wire electrical discharge machining (EDM) at Microcut Inc. to obtain so-called milli-tensile specimens. These tensile tests will be conducted in future work. Prior to wire EDM, samples were stress relieved at 1200 °C for 1 hour in a vacuum furnace at the Applied Research Lab at Penn State. Optical microscopy was done on a Nikon Epiphot 300 at the Applied Research Lab. SEM imaging was also done on the etched surface using a Tescan MIRA3 for higher resolution imaging of defects and increased depth of field. Vickers microhardness testing was done using a Leco M-400 hardness tester with a load of 100 g and a dwell time of 10 s. Ten (10) hardness measurements were taken on each etched sample, with care being taken to avoid areas of the surface with cracking. This was done to reduce variability between hardness measurements for a more reliable average hardness for each sample.

Chapter 4

Results and Discussion

Specimens Terminated During Processing

During the LPBF build, processing was closely monitored to watch for warping of TZM specimens and delamination from the build substrate. Processing was halted for any individual specimens which appeared to be distorting enough to jeopardize completion of the rest of the build. Because previously untested laser scan parameters were being used, and due to the complex geometry of test specimens being built, it was anticipated that some samples would require termination prior to completion of the build. Figure 5 shows an image of the specimens on the build substrate directly after processing. On the sides of some specimens, cracks can be seen running down the part. On specimens which successfully built to completion, the pins on the top 1 mm appeared to build with little to no visible problems. These features will be observed more closely when discussing optical microscopy of the samples.

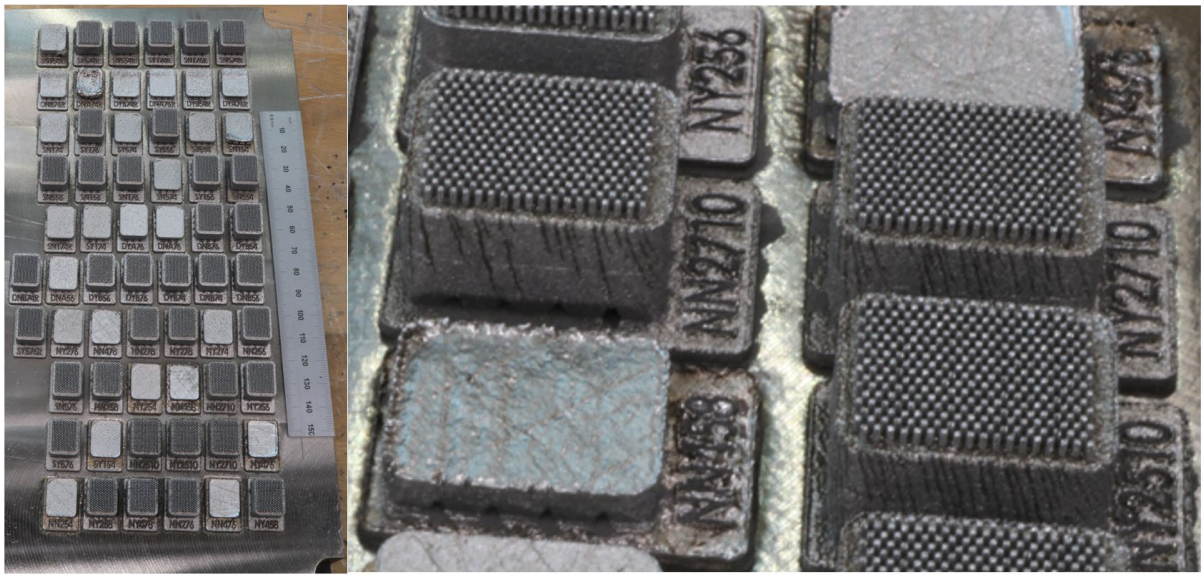

Figure 5: Image of all specimens on the build substrate (left) and a magnified image of some terminated and completed specimens (right).

Figure 6, figure 7, and figure 8 show which specimens were terminated early and which ones were successfully built, and plot each specimen according to its laser scan speed and volumetric energy density, which is calculated according to equation (1). From these figures, it can be observed that failure rates generally decreased as scan speed increased. This is consistent with the belief that slower scan speeds tend to input more heat into a part over the course of processing, which can increase the probability of severe warping due to thermal stresses building in the part. It is also worth noting that 100% of samples built at 600 mm/s with the short hatch infill strategy were completed without termination. Similarly, all 4 samples produced at 1000 mm/s with normal infill strategy were completed successfully.

Another notable observation from build results is that higher laser powers selected for certain infill strategies tended to fail at a much higher rate than lower laser powers. For example, among the normal exposure specimens only 3 out of 7 of the 400 W specimens were successfully built, and none of the specimens had the same laser parameters as another specimen. This

indicates a high amount of variability between different specimens with the same parameters at this laser power. With the double exposure specimens, not a single specimen of the 5 that used the 300 W exposure followed by 200 W exposure were successfully built. With low laser powers, however, the conditions improve. Of the 15 normal exposure specimens which were built at 250 W laser power, only 3 had to be terminated prior to completion. Of the 11 built using a 200 W exposure followed by 150 W exposure, only 3 were terminated. These observations are consistent phenomena observed with changing laser speed, i.e. higher laser power corresponds to higher heat input and therefore higher probability of distortion in parts.

Hatch spacing, on the other hand, did not appear to have an impact on sample terminations between 50 μm and 75 μm. This is likely due to the fact that the two values are optimized well enough for the LPBF system used in this investigation such that neither created residual stresses which were extreme enough to cause part warping. Finally, the type of infill strategy must be discussed with respect to part terminations. The most important observation is that no single set of parameters using the double exposure strategy had a 100% completion rate. Meanwhile, the normal exposure and short hatch infills each yielded similar success rates at 68% and 63%, respectively.

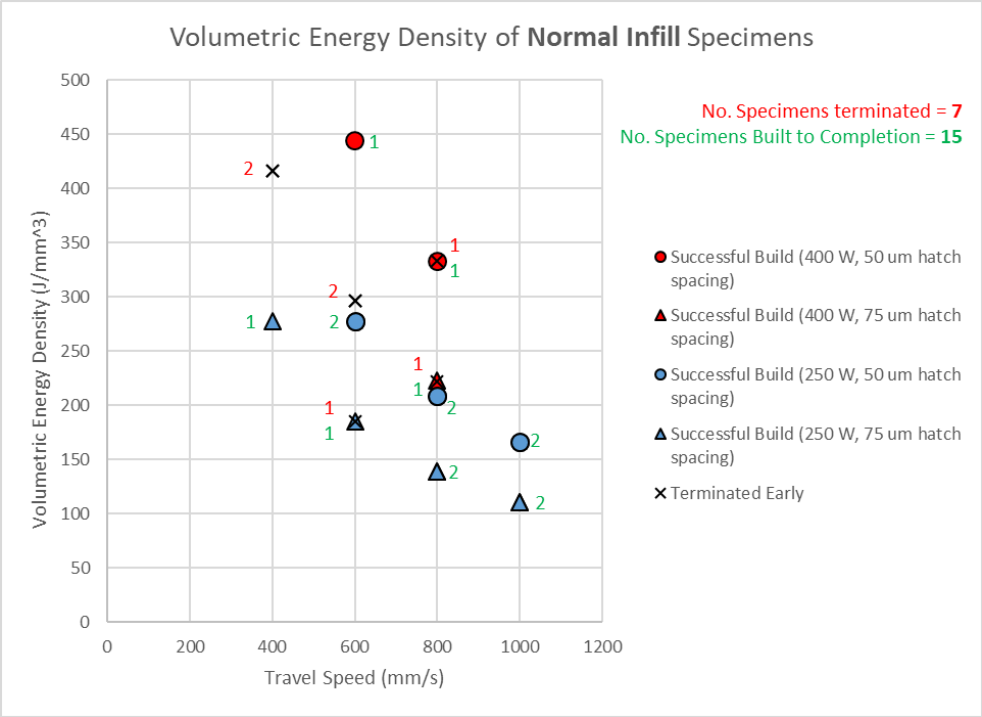

Figure 6: Terminated and completed normal exposure specimens plotted by laser travel speed and volumetric energy density.

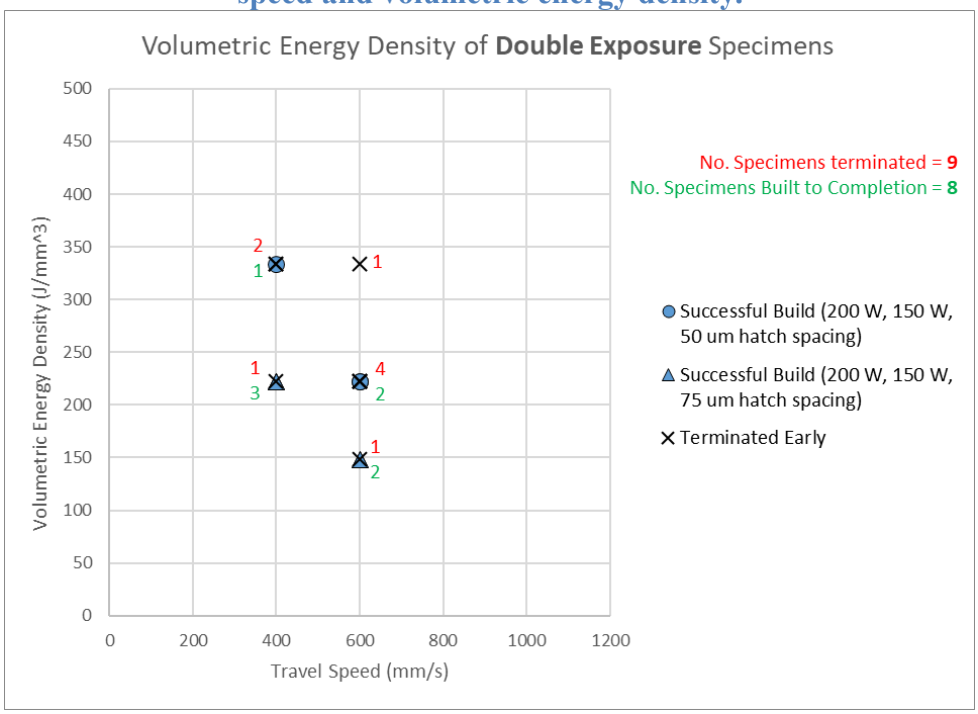

Figure 7: Terminated and completed double exposure specimens plotted by laser travel speed and volumetric energy density.

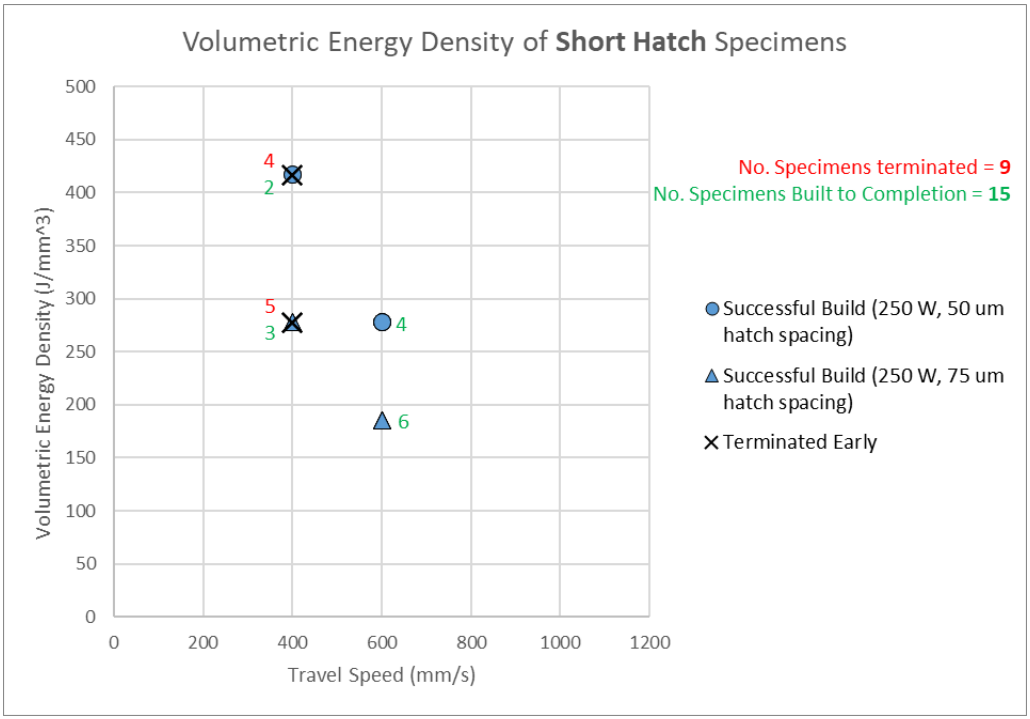

Figure 8: Terminated and completed short hatch specimens plotted by laser travel speed and volumetric energy density.

Laser parameter sets which had at least 2 successfully built specimens were selected for further characterization. This criterion was used to allow for adequate comparison between as-built specimens and those which were HIPed after processing. Results for HIP specimens are to be gathered in future work. Table 3 shows the laser parameters for each specimen selected for characterization.

Table 3: Laser parameters of specimens selected for further characterization.

Scan Strategy	Power (W)	Hatch Spacing (µm)	Scan Speed (mm/s)	Hatch Length (mm)	Volumetric Energy Density (J/mm^3)
Normal	250	50	1000	5	166.7
Normal	250	75	1000	5	111.1
Normal	250	50	800	5	208.3
Normal	250	75	800	5	138.9
Normal	250	50	600	5	277.8

Double	200, 150	75	600	5	148.1
Double	200, 150	50	600	5	222.2
Double	200, 150	75	400	5	222.2
Short Hatch	250	50	600	0.5	277.8
Short Hatch	250	75	600	0.5	185.2
Short Hatch	250	50	600	1	277.8
Short Hatch	250	75	600	1	185.2

Specimen Densities

Table 4 shows results of helium pycnometer measurements for each specimen according to laser parameters. Density was measured three times for each specimen and the average across all three trials is reported. The relative density was calculated by dividing the measured density by the theoretical density of 10.16 g/cm^3 as reported in literature [2]. All specimens were at least 98% dense, but the highest density achieved from these specimens was 99.76%, which used the normal infill strategy, a laser power of 250 W, a hatch spacing of 75 µm, and a scan speed of 800 mm/s. This just slightly higher than the maximum density reported by Kaserer et al. for LPBF TZM [2].

Table 4: Average density for each set of laser parameters.

Scan Strategy	Power (W)	Hatch Spacing (µm)	Scan Speed (mm/s)	Hatch Length (mm)	Volumetric Energy Density (J/mm^3)	Average Density (g/cm^3)	Relative Density (%)
Normal	250	50	1000	5	166.7	10.1078	99.49
Normal	250	75	1000	5	111.1	10.0957	99.37
Normal	250	50	800	5	208.3	10.1235	99.64
Normal	250	75	800	5	138.9	10.1359	99.76
Normal	250	50	600	5	277.8	10.046	98.88
Double	200, 150	75	600	5	148.1	10.1172	99.58

Double	200, 150	50	600	5	222.2	10.118	99.59
Double	200, 150	75	400	5	222.2	10.0162	98.58
Short Hatch	250	50	600	0.5	277.8	10.1007	99.42
Short Hatch	250	75	600	0.5	185.2	9.9982	98.41
Short Hatch	250	50	600	1	277.8	10.0431	98.85
Short Hatch	250	75	600	1	185.2	10.0888	99.30

Figure 9 shows the measured density of each specimen according to its calculated volumetric energy density. There appears to be little correlation between density and energy density of applied laser parameters, but if focus is shifted to just one parameter from the energy density in equation (1), a pattern emerges. Figure 10 shows the measured density of each specimen according to the laser scan speed. In this plot, it can be seen that the density is highest for normal exposure specimens that used 800 mm/s scan speed, while any higher or lower scan speeds seem to produce lower densities. This is possibly due to the fact that at higher laser scan speeds some lack of fusion porosity is created by the laser not completely melting the powder bed and fusing it with previous layers. Meanwhile, at lower scan speeds the laser could be inputting an excessive amount of energy into the specimen and causing keyhole porosity.

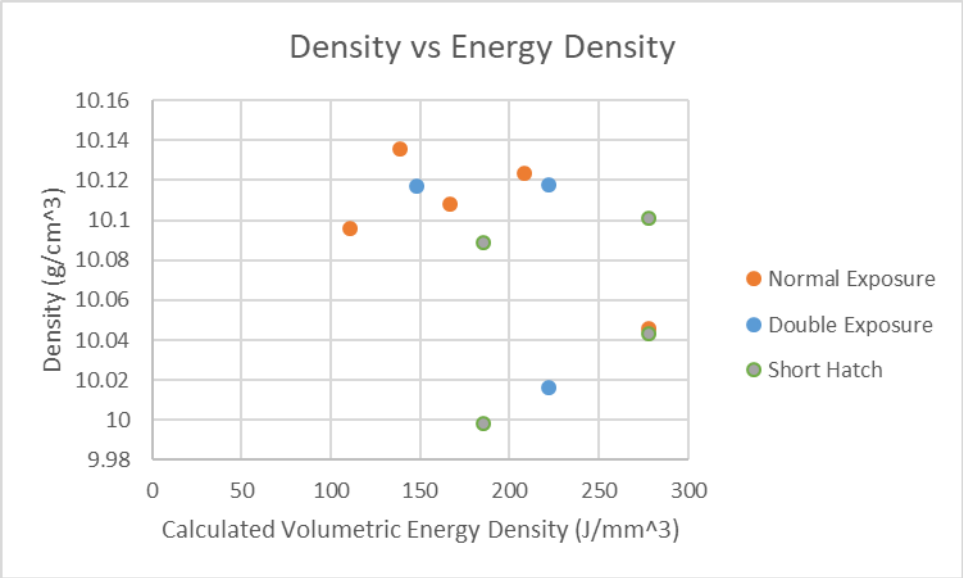

Figure 9: Measured density versus energy density.

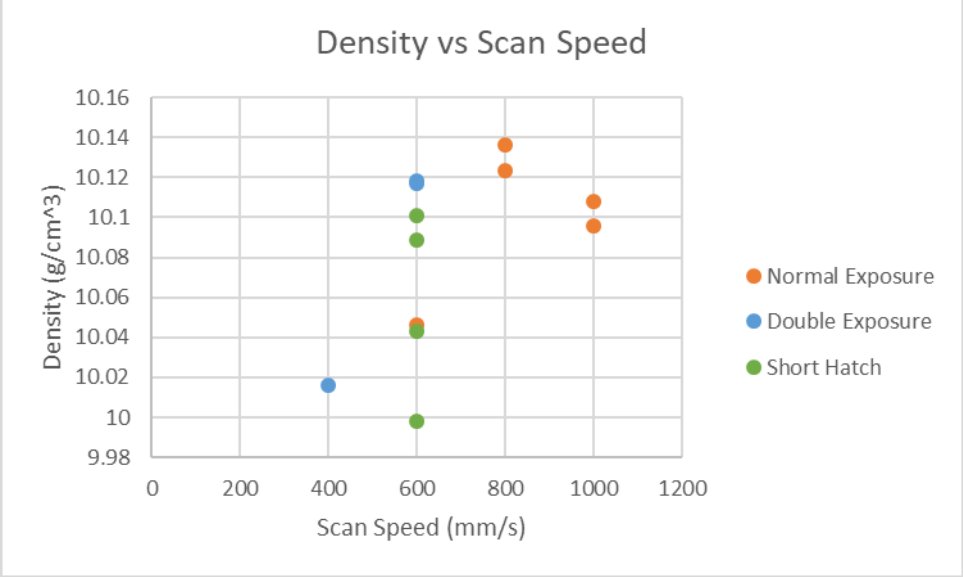

Figure 10: Measured density versus laser scan speed.

Optical Microscopy

In order to assess the microstructure, fine features, and defects in each sample, optical microscopy was performed. First, polished and unetched specimens were observed for

defects and to look closer at the pins on each specimen. Figure 11 shows a comparison between the pins on a normal infill, double exposure, and short hatch specimen. The build direction is pointing upward for all microscopy images taken in this investigation. Most irregularities in the pins are likely due to damage during the sectioning and mounting process, but one notable characteristic in the pins is that most of them exhibit cracking at their base where they connect to the rest of the specimen. This is likely due to a combination of accumulating residual stresses from heat and the sharp corners typically present at the interface between the pins and the surface of the specimen which create stress concentrations. Introduction of a fillet to the design would reduce the stress riser and may reduce cracking.

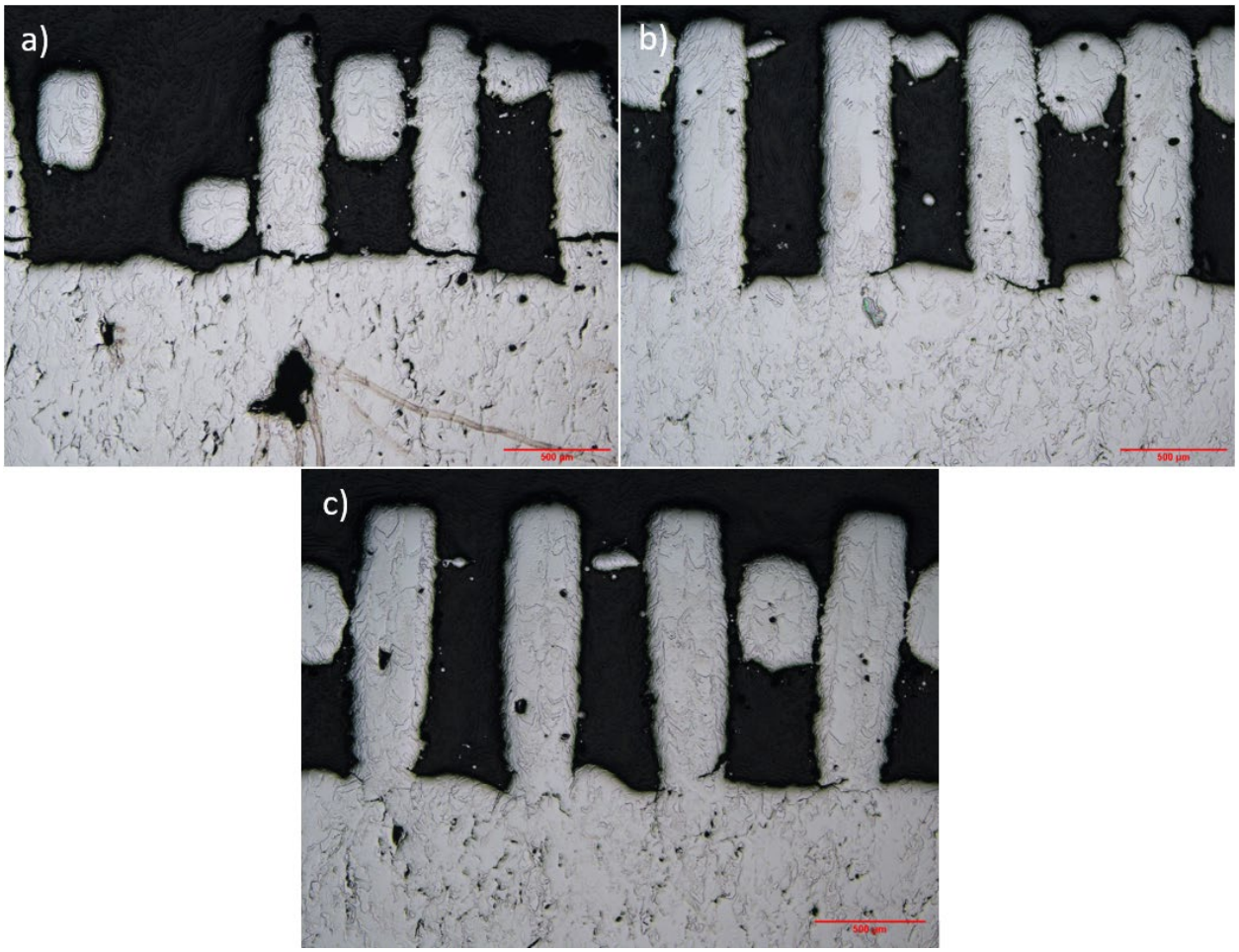

Figure 11: Unetched micrographs of pins for a) normal exposure, b) double exposure, and c) short hatch specimens (Scale bars are 500 µm).

After, looking at unetched specimens, they were etched to reveal grain structure and observed at a higher magnification. Figure 12 shows the etched microstructure for each infill strategy using comparable laser parameters. The build direction is directed upwards in each image. The normal infill specimen was produced using 250 W laser power, 50 µm hatch spacing, and 600 mm/s scan speed. The double infill specimen used the same parameters except for a 1st exposure power of 200 W, and 2nd exposure power of 150 W. The short hatch specimen is also using a similar set of parameters to the normal infill one, except for a hatch length of 1 mm rather than 5 mm. Despite having the highest measured density of the three specimens, the

double exposure specimen interestingly had the most severe porosity of the three. This means that it had the largest and highest quantity of pores. The porosity is most likely from lack of fusion as the double exposure parameters had lower laser power than the other specimens for both exposures. Thus, the powder might not have been able to completely melt and fuse to previous layers during either exposure. A similarity shared between all specimens in this study is the tortuous grain boundary structure observed in every as-built microstructure. This is likely because a 67° laser scan rotation was done between layers, causing grains to be unable to grow directly upward in the build direction. This is consistent with behavior seen in previous literature [2,5].

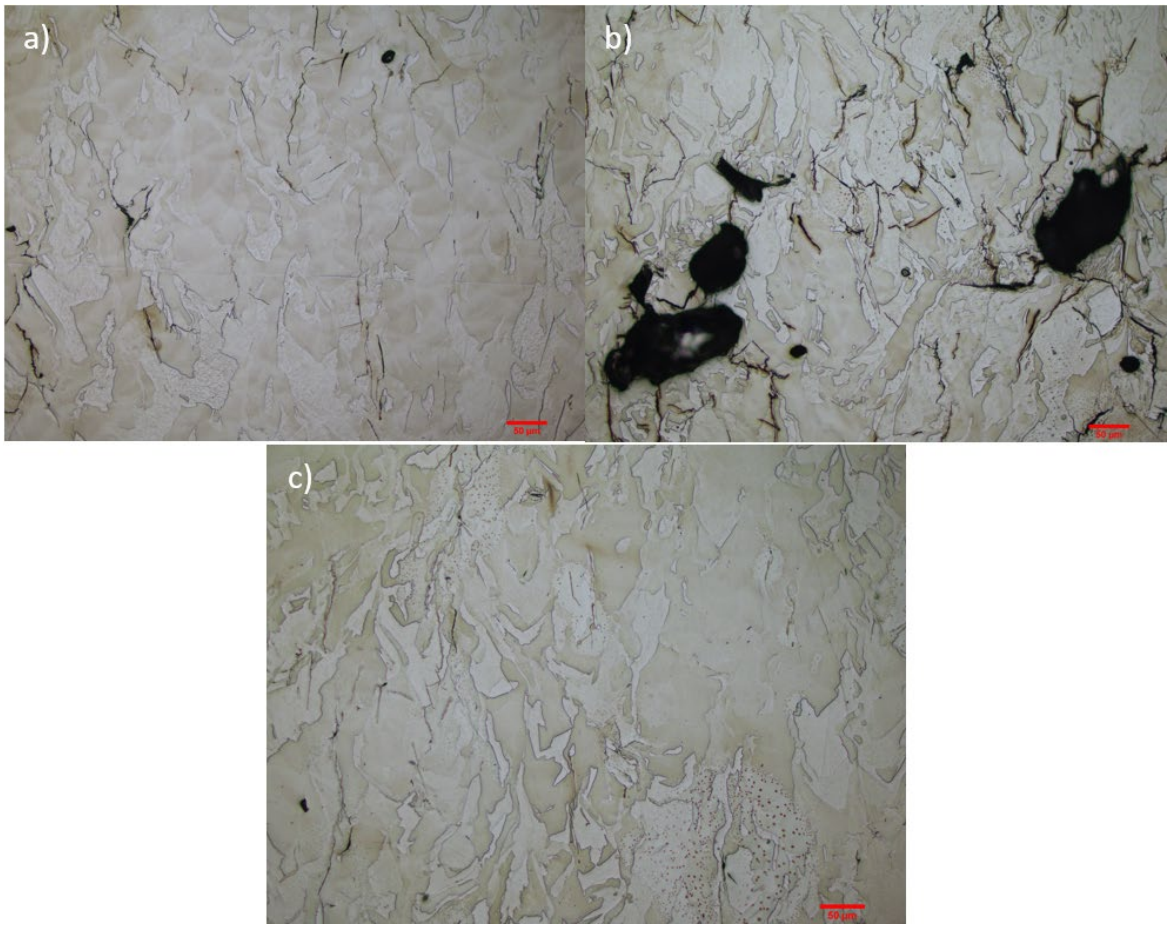

Figure 12: Microstructures of a) normal exposure, b) double exposure, and c) short hatch specimens (Scale bars are 50 µm).

Every specimen on which microscopy was performed exhibited microcracking. Between the 3 specimens in figure 12, the double exposure specimen had the most cracking, while the normal and short hatch specimens showed comparable amounts of cracking. Cracking did not appear to mostly follow grain boundaries as has been observed previously in Mo, and it instead followed predominantly straight paths through grains and followed along grain boundaries when they aligned with these relatively straight paths. The cracks observed in specimens are most likely solidification cracks, which means they formed due to accumulation of residual stresses as the material shrank during solidification of the melt pool.

Figure 13 shows two optical micrographs taken from two etched short hatch samples which had identical laser parameters with the exception of hatch spacing. One was processed with 50 μm hatch spacing while the other was processed with a 75 μm hatch spacing. Both samples used a 250 W laser, 600 mm/s scan speed, and 1 mm hatch length. These micrographs demonstrate that the only noticeable difference between each hatch spacing is a marginal change in microcracking. This is the case for all samples examined in this investigation. Based on the micrographs, the lower hatch spacing of 50 μm may be beneficial for use on future specimens as it lowers the chance of lack of fusion porosity, while also not inputting too much energy into samples that can lead to excessive distortion and part failure. Recall that 100% of short hatch specimens processed with 250 W laser power and 600 mm/s scan speed built successfully without the need for termination.

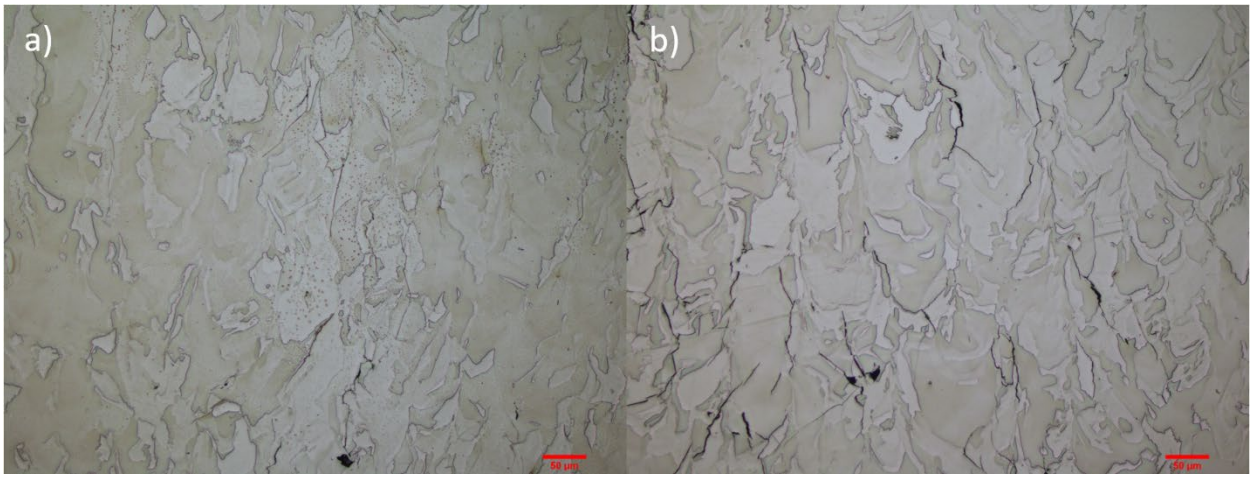

Figure 13: Two short hatch specimens with a) 50 µm and b) 75 µm hatch spacing.

To continue comparing specific laser parameters, figure 14 compares between the 5 mm, 1 mm and 0.5 mm hatch lengths used. Each of these samples shared the same laser power of 250 W, 600 mm/s scan speed, and 50 µm hatch spacing. The 1 mm and 0.5 mm hatch lengths are considered short hatch specimens and the 5 mm hatch length parts are considered normal exposure specimens. Here, the most distinct difference between each sample appears to be the thickness of certain parts of the grains in each sample. Quantitative grain size measurements were not used in this investigation due to both the extremely irregular shapes taken on by grains as well as the reduced grain orientation contrast produced by the etchant. Both of these factors would likely make automatic detection of grains via contrast thresholding extremely difficult, and time-intensive grain tracing would be required to be done by hand. This was outside of the time-constraints of the current investigation, and therefore it was not done. That being said, some qualitative assessments can be made about grain size and morphology. One observation which can be made is that as the hatch length decreases, elements of each grain appear to become finer and more tortuous.

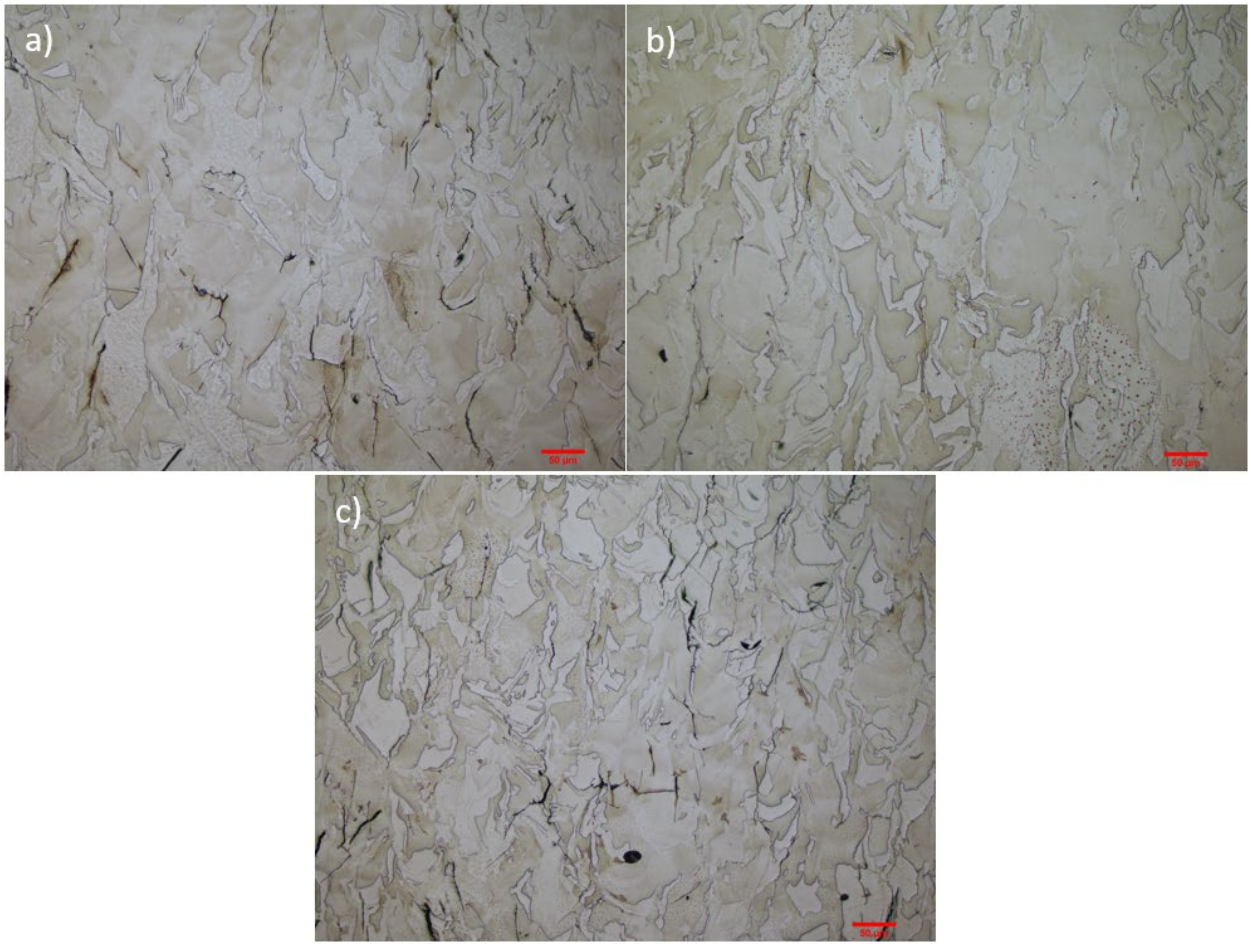

Figure 14: Three specimens with a) 5 mm, b) 1 mm, and c) 0.5 mm hatch length.

Finally, figure 15 shows a comparison between different laser scan speeds. Each specimen was again processed with all other laser parameters being the same. Each one was built with the normal exposure infill strategy, meaning 5 mm hatch length. Each sample utilized a 250 W laser power and 50 µm hatch spacing. The sample built at 1000 mm/s showed severe cracking, while the sample which used 800 mm/s scan speed had some extremely large pores (the scale bar is 50 µm). The 600 mm/s sample only showed the microcracking typical of samples shown in this work.

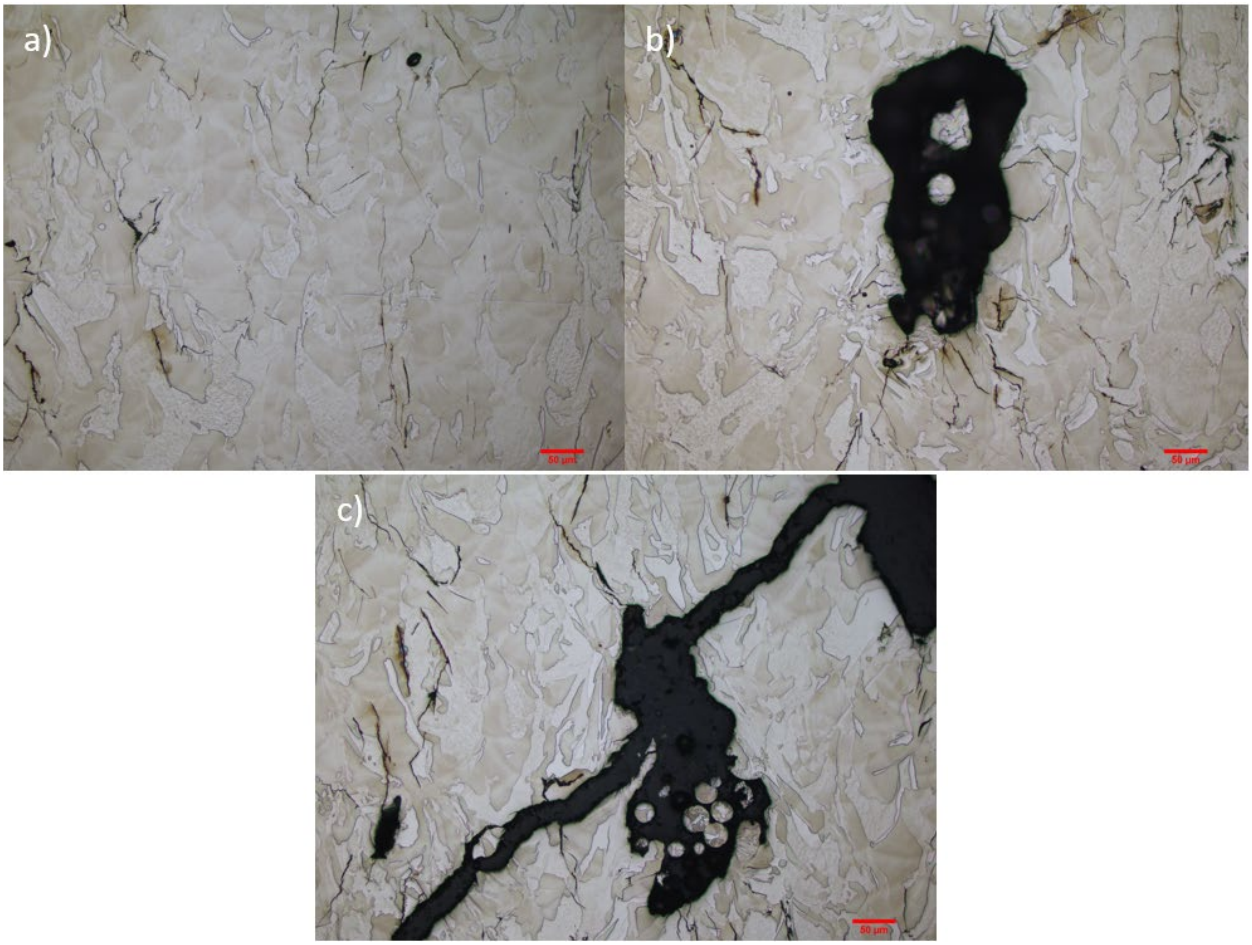

Figure 15: Three normal exposure specimens processed with a) 600 mm/s, b) 800 mm/s, and c) 1000 mm/s scan speed.

Microhardness Testing

Vickers hardness testing was performed to provide a comparison with hardness of TZM presented in the literature. The results of Vickers hardness testing are provided in Figure 18, Figure 19, and Table 6. When comparing the complete set of measurements from each infill strategy, it appears that the normal exposure strategy has the highest average hardness, compared to the short hatch strategy which appeared to have the lowest. This is somewhat surprising considering that the short hatch specimens appeared to have finer features in the grains, which

should result in dislocations having shorter distances to travel before hitting a grain boundary. Thus, one would expect the short hatch specimens to better resist plastic deformation and have higher hardness.

As for laser scan speed, Figure 12 and Figure 19 appear to have extremely similar shapes to their graphs as a function of laser scan speed. This means that there could in fact be a correlation between relative density and microhardness of the sample. It could be possible that the relative density directly affected the measured microhardness of each sample, however this would be unexpected as measurement locations were intentionally chosen to be far from cracking and porosity within the samples. In previous work with LPBF of TZM, an average hardness of 264 HV was found, which is significantly lower than values measured in this study [2]. That study used a load of 10 Kg, which would create a significantly larger indentation then those created with the 100 g of force used in this study. As a result, the authors of that paper likely could not avoid testing areas with cracks or other defects, and this meant that hardness values would be drastically decreased.

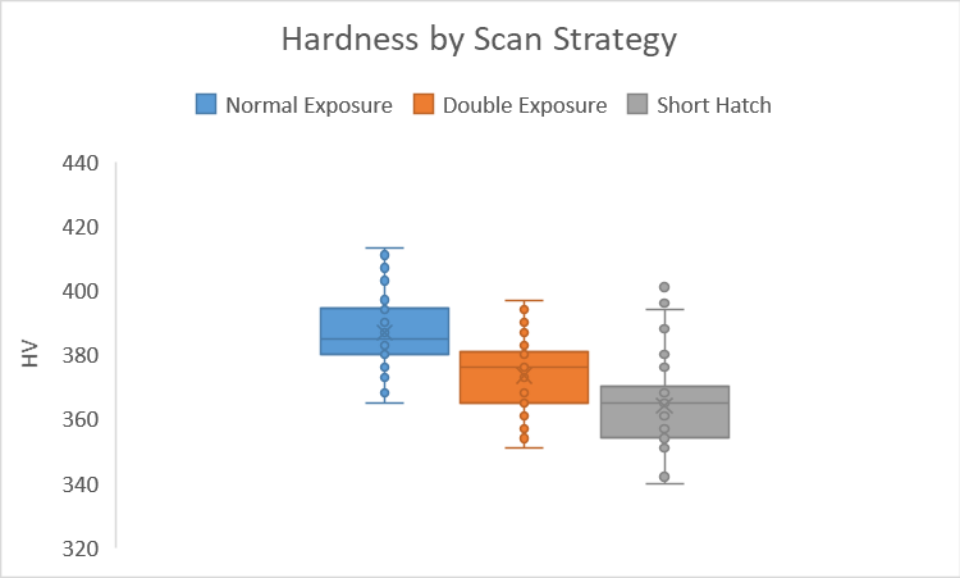

Figure 16: Vickers hardness plotted by infill strategy.

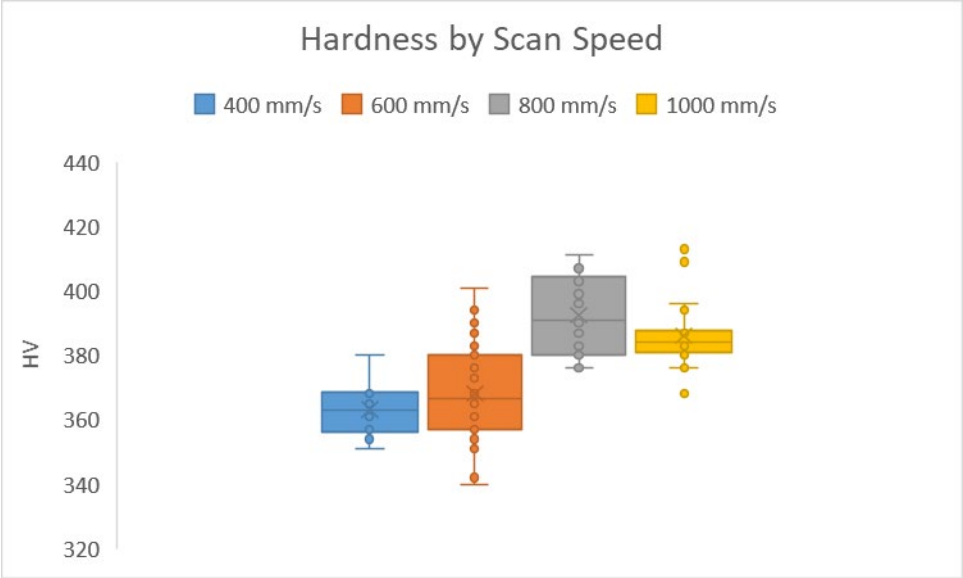

Figure 17: Vickers hardness plotted by scan speed.

Table 5: Average and standard deviation of Vickers hardness provided for each set of laser parameters tested.

Infill Strategy	Laser Power (W)	Hatch Spacing (um)	Travel Speed (mm/s)	Hatch Length (mm)	Calculated Volumetric Energy Density (J/mm^3)	Average Vickers Hardness (HV)	Standard Deviation for Hardness (HV)
Normal Exposure	250	50	600	5	277.8	377	8.18
Normal Exposure	250	50	800	5	208.3	400	10.7
Normal Exposure	250	50	1000	5	166.7	388	10.5
Normal Exposure	250	75	800	5	138.9	385	7.81
Normal Exposure	250	75	1000	5	111.1	384	10.4
Double Exposure	200, 150	50	600	5	222.2	375	10.3
Double Exposure	200, 150	75	400	5	222.2	363	8.77
Double Exposure	200, 150	75	600	5	148.1	383	9.53
Short Hatch	250	50	600	0.5	277.8	368	15.5
Short Hatch	250	75	600	0.5	185.2	374	17.0
Short Hatch	250	50	600	1	277.8	351	6.60
Short Hatch	250	75	600	1	185.2	364	9.92

Scanning Electron Microscopy

Etched samples were examined using scanning electron microscopy (SEM) to look at cracking and porosity under a much higher magnification and resolution than optical microscopy. Additionally, SEM has a larger depth of field which allows for imaging of deeper defects that optical microscopy is unable to completely capture. Also, using the wide field imaging mode was proven to be useful in assessing the amount of porosity and cracks present across the entire cross section of samples. For example, figure 18 nicely illustrates the difference between two samples that have identical processing parameters with the exception of scan speed. The build direction in all of these images is again pointing up. Each sample was processed using normal infill strategy, 250 W laser power, 50 μm hatch spacing, and 5 mm hatch length. However, a) was processed with 1000 mm/s scan speed and b) was processed with 600 mm/s scan speed. The sample in a) is filled with porosity and large cracks running through the part, while b) has very few defects which can be seen at this magnification.

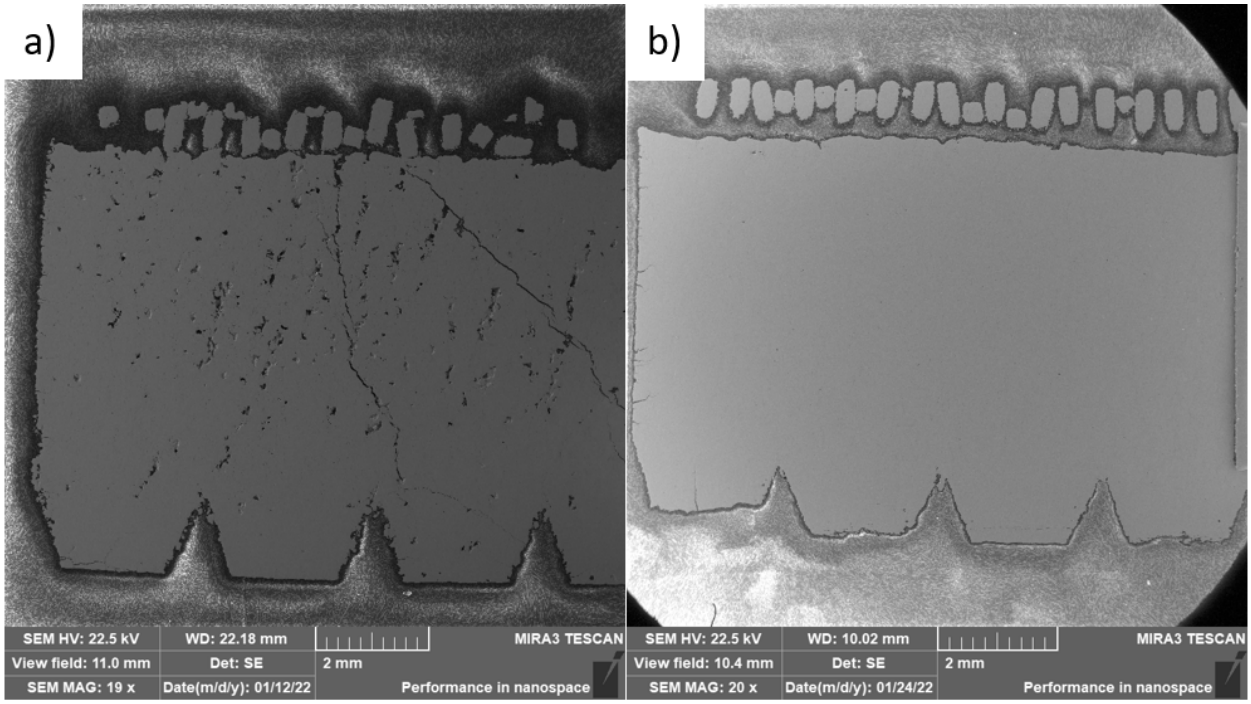

Figure 18: Wide field SEM images taken of a sample processed with a) 1000 mm/s and b) 600 mm/s scan speed.

A large quantity of samples built during this investigation exhibited cracking at the side surfaces, which could likely be attributed to less optimized laser parameters for the contour scans around the perimeter of the samples. Figure 19 shows one of these cracks from the 600 mm/s sample at a higher magnification. An example of porosity present in the 1000 mm/s sample can be found in figure 20. This pore contains what appear to be unmelted powder particles which, along with the pore's irregular shape, seems to indicate that this pore is a lack of fusion defect. This means that a 1000 mm/s scan speed is not slow enough to completely melt the powder bed on each pass.

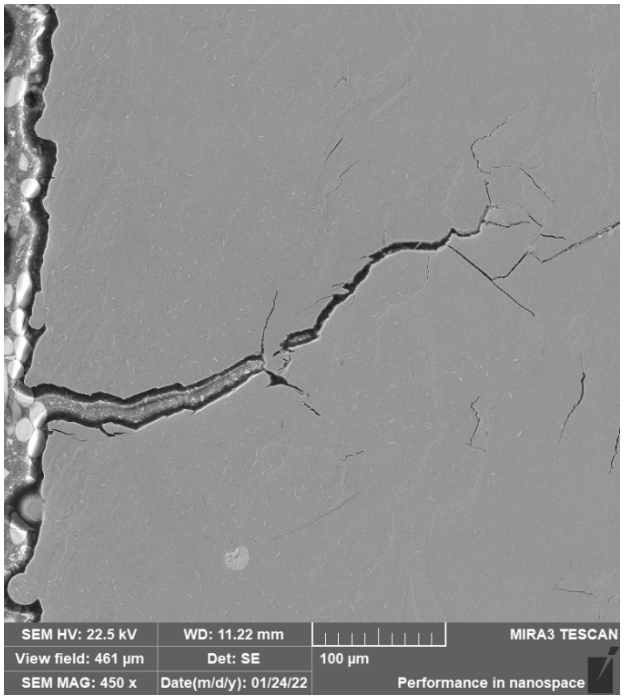

Figure 19: SEM image of a crack on the side of a sample.

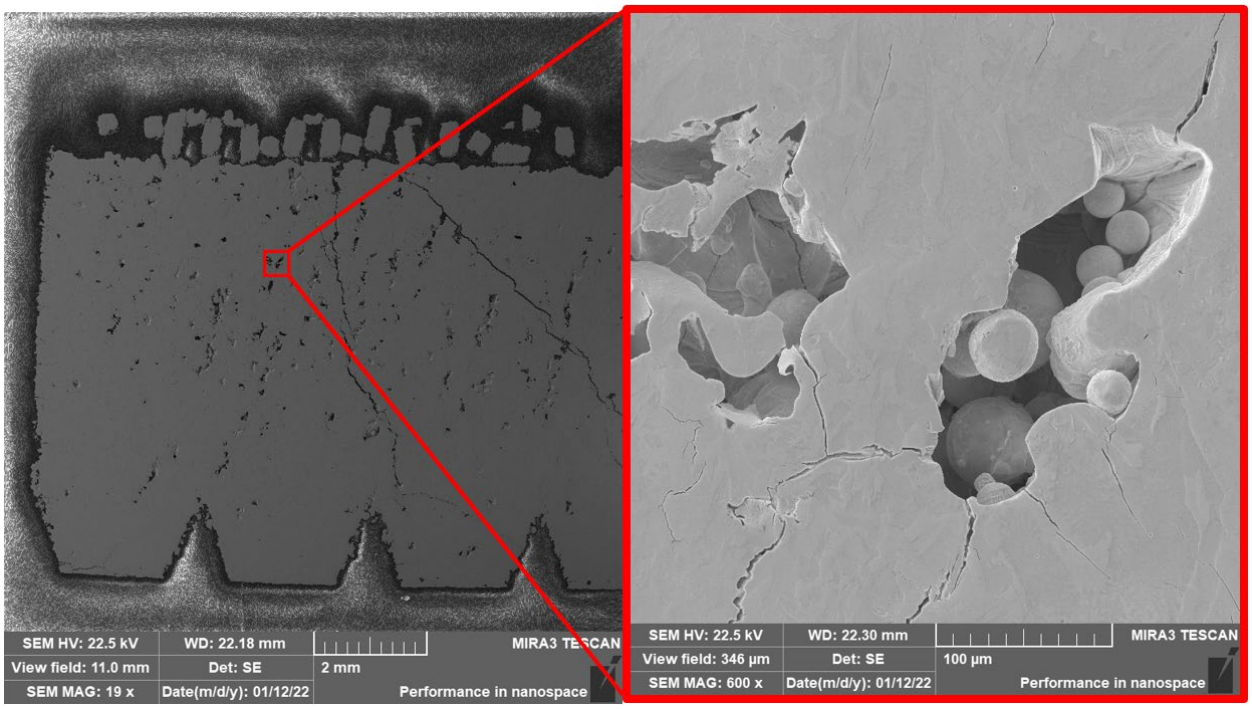

Figure 20: High magnification SEM image of a lack of fusion pore in a sample.

Chapter 5

Conclusions

In this investigation, novel laser processing strategies for LBPF of TZM Mo alloy were explored to examine the printability of this alloy. In order to assess the effectiveness of these novel processing strategies, it must first be determined whether there is any benefit in deviating from use of the normal exposure infill strategy for LPBF when processing TZM. The double exposure strategy is not a beneficial technique to use for this particular purpose. It had a relatively high failure rate of about 53%, and not a single set of parameters successfully finished every sample without any early terminations. Also, double exposure specimens displayed a higher level of cracking and porosity compared to specimens with similar parameters. For the short hatch strategy, however, the story is different. All of specimens built with this infill strategy at 600 mm/s laser scan speed successfully built to completion. The same cannot be said for the normal exposure specimens, however 100% of those specimens built at 250 W laser power, 800 and 1000 mm/s scan speed were successful. The issue is that these specimens were largely filled with pores and cracking. The short hatch specimens exhibited less porosity and a comparable amount of cracking to the normal exposure strategy at 600 mm/s. Furthermore, the normal infill and short hatch specimens had similar build success rates of 68% and 63%, respectively, so the two infill strategies are certainly comparable in their effectiveness. Though additional optimization would be necessary for both scan strategies to achieve completely defect free processing, the results of this work suggest that the short hatch strategy is a viable candidate for further optimization, testing, and characterization.

For scan speed, power, hatch spacing, and hatch length, some specific conclusions can be drawn. The optimal range for laser scan speeds which results in minimal defects appears to be somewhere between 600 and 800 mm/s. A scan speed of 600 mm/s seems to result in a microstructure that is mostly free of large pores, but overall hardness and density are slightly lower than the sample built at 800 mm/s, which appears to have larger lack of fusion pores than 600 mm/s. For laser scan power, all powers higher than 250 W used in this investigation proved to be largely unsuccessful due to high build failure rates due to warping from excessive heat input. For this reason, lower powers around 250 W seem to be more effective. Variability in results with varying hatch spacing for this investigation were mostly inconclusive, meaning that 50 µm and 75 µm hatch spacing are both in the acceptable range for effective processing. That being said, a 50 µm hatch spacing may be more advantageous to continue investigations, as this likely has a lower probability of forming lack of fusion porosity than 75 µm hatch spacing due to more overlap between adjacent scan tracks. Finally, the greatest impact hatch length seemed to have on specimens was in the morphology of grains. Smaller hatch lengths appeared to create finer features in grains and more tortuous grain boundaries. Until tensile tests are performed, it is unclear whether this has an appreciable impact on properties, but the hardness of specimens tended to actually decrease from the normal infill to short hatch specimens. From this investigation, the most effective parameters found turned out to have be a laser power of 250 W, a scan speed of 600 mm/s, a hatch spacing of 50 µm, and a hatch length ranging from 0.5 mm to 5 mm.

All specimens characterized in this work exhibited some level of microcracking, and exhibited large cracks extending across the length of the part. The majority of cracking observed in the TZM specimens is believed to be solidification cracking caused by the accumulation of

residual stresses in the melt pool during the process of solidification. Though none of the novel processing strategies completely eliminated microcracks, various process conditions were able to nearly eliminate voids and porosity and produce multiple components with greater than 99.0% density.

Despite the use of novel laser parameters, the somewhat complex geometries present in the samples built during this investigation could still be processed successfully. The pins on the top surface of each specimen did not present much difficulty for the machine to process to completion, however accumulation of stresses did appear to cause cracking around sharp corners at the base of the pins. The support structures did not appear to be completely successful in their attempt to maintain elevated sample temperatures by minimizing conductive heat loss to the build substrate, as evidenced by the cracking observed in all samples. However, they were built with a relatively high success rate. As seen with the pins, sharp corners in the support structures did appear to create stress risers that occasionally initiated cracking. The results of this investigation show that, with further optimization, defect free printing of TZM is possible with novel laser processing parameters.

Chapter 6

Future Work

Future work on LPBF of TZM should include investigating the effect of post process hot isostatic pressing (HIP) on the microstructure, porosity, cracking, and properties of TZM. In addition to the characterization done here, further work is planned to perform tensile testing on the LPBF TZM specimens to determine what—if any—effect laser parameters have on tensile strength and ductility of TZM. Further work is required to determine whether there are any methods capable of eliminating cracking in TZM without excessive heating of the build substrate. Future work should include investigating the effect of grain refiners, and physics-based process modeling to further optimize processing parameters for reducing cracking. Once the parameters are optimized for infill, further experiments can be run to determine the optimal parameters for other types of laser scans such as contours, upskin, and downskin. Finally, in the interest of sustainability, it would be beneficial to determine how reusable unsintered TZM powder is from previous builds. Characterizing powder after a series of cycles would be beneficial to determine whether there is any degradation in powder quality with reuse.

Appendix A

Table of laser parameters

Infill Strategy	Laser Power (W)	Hatch Spacing (um)	Travel Speed (mm/s)	Hatch Length (mm)	Calculated Volumetric Energy Density (J/mm^3)	Built to completion
Normal Exposure	250	50	400	5	416.7	No
Normal Exposure	250	50	600	5	277.8	Yes
Normal Exposure	250	50	800	5	208.3	Yes
Normal Exposure	250	50	1000	5	166.7	Yes
Normal Exposure	250	75	400	5	277.8	Yes
Normal Exposure	250	75	600	5	185.2	No
Normal Exposure	250	75	800	5	138.9	Yes
Normal Exposure	250	75	1000	5	111.1	Yes
Normal Exposure	400	50	600	5	444.4	Yes
Normal Exposure	400	50	800	5	333.3	No
Normal Exposure	400	75	600	5	296.3	No
Normal Exposure	400	75	800	5	222.2	Yes
Normal Exposure	250	50	400	5	416.7	No
Normal Exposure	250	50	600	5	277.8	Yes
Normal Exposure	250	50	800	5	208.3	Yes
Normal Exposure	250	50	1000	5	166.7	Yes
Normal Exposure	250	75	600	5	185.2	Yes
Normal Exposure	250	75	800	5	138.9	Yes
Normal Exposure	250	75	1000	5	111.1	Yes
Normal Exposure	400	50	800	5	333.3	Yes
Normal Exposure	400	75	600	5	296.3	No
Normal Exposure	400	75	800	5	222.2	No
Double Exposure	300, 200	75	600	5	222.2	No
Double Exposure	200, 150	50	400	5	333.2	Yes
Double Exposure	200, 150	50	600	5	222.2	Yes

Double Exposure	200, 150	75	400	5	222.2	Yes
Double Exposure	200, 150	75	600	5	148.1	Yes
Double Exposure	300, 200	50	600	5	333.3	No
Double Exposure	300, 200	75	600	5	222.2	No
Double Exposure	200, 150	50	600	5	222.2	Yes
Double Exposure	200, 150	75	400	5	222.2	Yes
Double Exposure	200, 150	75	600	5	148.1	Yes
Double Exposure	300, 200	75	600	5	222.2	No
Double Exposure	200, 150	50	400	5	333.3	No
Double Exposure	200, 150	75	400	5	222.2	No
Double Exposure	300, 200	75	400	5	333.3	No
Double Exposure	300, 200	75	600	5	222.2	No
Double Exposure	200, 150	75	400	5	222.2	Yes
Double Exposure	200, 150	75	600	5	148.1	No
Short Hatch	250	50	400	0.5	416.7	No
Short Hatch	250	50	600	0.5	277.8	Yes
Short Hatch	250	75	400	0.5	277.8	No
Short Hatch	250	75	600	0.5	185.2	Yes
Short Hatch	250	50	400	1	416.7	No
Short Hatch	250	50	600	1	277.8	Yes
Short Hatch	250	75	400	1	277.8	No
Short Hatch	250	75	600	1	185.2	Yes
Short Hatch	250	50	400	0.5	416.7	Yes
Short Hatch	250	50	600	0.5	277.8	Yes
Short Hatch	250	75	400	0.5	277.8	No
Short Hatch	250	75	600	0.5	185.2	Yes
Short Hatch	250	50	400	1	416.7	No
Short Hatch	250	50	600	1	277.8	Yes
Short Hatch	250	75	400	1	277.8	No
Short Hatch	250	75	600	1	185.2	Yes
Short Hatch	250	75	400	0.5	277.8	Yes
Short Hatch	250	75	600	0.5	185.2	Yes
Short Hatch	250	75	400	1	277.8	Yes
Short Hatch	250	50	400	0.5	416.7	Yes
Short Hatch	250	75	400	0.5	277.8	Yes

Short Hatch	250	50	400	1	416.7	No
Short Hatch	250	75	400	1	277.8	No
Short Hatch	250	75	600	1	185.2	Yes

References

[1] J. Braun, L. Kaserer, J. Stajkovic, K.H. Leitz, B. Tabernig, P. Singer, P. Leibenguth, C. Gspan, H. Kestler, G. Leichtfried, Molybdenum and tungsten manufactured by selective laser melting: Analysis of defect structure and solidification mechanisms, Int. J. Refract. Met. Hard Mater. 84 (2019) 104999. https://doi.org/10.1016/j.ijrmhm.2019.104999.

[2] L. Kaserer, J. Braun, J. Stajkovic, K.H. Leitz, P. Singer, I. Letofsky-Papst, H. Kestler, G. Leichtfried, Microstructure and mechanical properties of molybdenum-titanium-zirconium-carbon alloy TZM processed via laser powder-bed fusion, Int. J. Refract. Met. Hard Mater. 93 (2020) 105369. https://doi.org/10.1016/j.ijrmhm.2020.105369.

[3] M. Higashi, T. Ozaki, Selective laser melting of pure molybdenum: Evolution of defect and crystallographic texture with process parameters, Mater. Des. 191 (2020) 108588. https://doi.org/10.1016/j.matdes.2020.108588.

[4] D. Faidel, D. Jonas, G. Natour, W. Behr, Investigation of the selective laser melting process with molybdenum powder, Addit. Manuf. 8 (2015) 88–94. https://doi.org/10.1016/j.addma.2015.09.002.

[5] D. Wang, C. Yu, J. Ma, W. Liu, Z. Shen, Densification and crack suppression in selective laser melting of pure molybdenum, Mater. Des. 129 (2017) 44–52. https://doi.org/10.1016/j.matdes.2017.04.094.

[6] L. Kaserer, J. Braun, J. Stajkovic, K.H. Leitz, B. Tabernig, P. Singer, I. Letofsky-Papst, H. Kestler, G. Leichtfried, Fully dense and crack free molybdenum manufactured by Selective Laser Melting through alloying with carbon, Int. J. Refract. Met. Hard Mater. 84

(2019) 105000. https://doi.org/10.1016/j.ijrmhm.2019.105000.

[7] J. Braun, L. Kaserer, I. Letofsky-Papst, K.H. Leitz, H. Kestler, G. Leichtfried, On the role of carbon in molybdenum manufactured by Laser Powder Bed Fusion, Int. J. Refract. Met. Hard Mater. 92 (2020) 105283. https://doi.org/10.1016/j.ijrmhm.2020.105283.

[8] J. Wadsworth, G.R. Morse, P.M. Chewey, The microstructure and mechanical properties of a welded molybdenum alloy, Mater. Sci. Eng. 59 (1983) 257–273. https://doi.org/10.1016/0025-5416(83)90173-8.

[9] J. Ning, K.M. Hong, G. V. Inamke, Y.C. Shin, L.J. Zhang, Analysis of microstructure and mechanical strength of lap joints of TZM alloy welded by a fiber laser, J. Manuf. Process. 39 (2019) 146–159. https://doi.org/10.1016/j.jmapro.2019.02.015.

[10] M.X. Xie, Y.X. Li, X.T. Shang, X.W. Wang, J.Y. Pei, Effect of heat input on porosity defects in a fiber laser welded socket-joint made of powder metallurgy molybdenum alloy, Materials (Basel). 12 (2019). https://doi.org/10.3390/ma12091433.

[11] G.S. Hanks, Welding of TZM Molybdenum Alloy, Los Alamos, New Mexico, 1970.

[12] S.P. Chakraborty, N. Krishnamurthy, A study of electron beam welding of Mo based TZM alloy, 2013.

[13] J. Warren, G. Reznikov, A COMPARISON OF THE MICROSTRUCTURE AND HIGH TEMPERATURE TENSILE PROPERTIES OF A NOVEL P/M Mo-Hf-Zr-Ta-C ALLOYS AND TZM, 15th Int. Plansee Semin. 4 (2001) 79–96. http://www.iaea.org/inis/collection/NCLCollectionStore/_Public/33/060/33060924.pdf.

[14] B. V. Cockeram, The mechanical properties and fracture mechanisms of wrought low carbon arc cast (LCAC), molybdenum-0.5pct titanium-0.1pct zirconium (TZM), and oxide dispersion strengthened (ODS) molybdenum flat products, Mater. Sci. Eng. A. 418 (2006)

120–136. https://doi.org/10.1016/j.msea.2005.11.030.

[15] K. Abe, T. Masuyama, M. Satou, M.L. Hamilton, Neutron Irradiation Damage and Void Lattice Formation in a Molybdenum Alloy TZM, Mater. Trans. JIM. 34 (1993). https://doi.org/10.2320/matertrans1989.34.1137.

[16] J. Chen, K. Li, Y. Wang, L. Xing, C. Yu, H. Liu, J. Ma, W. Liu, Z. Shen, The effect of hot isostatic pressing on thermal conductivity of additively manufactured pure tungsten, Int. J. Refract. Met. Hard Mater. 87 (2020) 105135. https://doi.org/10.1016/j.ijrmhm.2019.105135.

[17] J. Barranco, I. Ahmad, S. Isserow, R. Warenchak, The Densification of Molybdenum and Molybdenum Alloy Powders Using Hot Isostatic Pressing., (1985). http://oai.dtic.mil/oai/oai?verb=getRecord&metadataPrefix=html&identifier=ADA159886.

[18] S. Majumdar, I.G. Sharma, Development of Mo base TZM (Mo-0.5Ti-0.1Zr-0.02C) alloy and its shapes, BARC Newsl. (2010). https://doi.org/10.1163/157338402x00179.

[19] M.C. Brennan, J.S. Keist, T.A. Palmer, Defects in Metal Additive Manufacturing Processes, J. Mater. Eng. Perform. 30 (2021) 4808–4818. https://doi.org/10.1007/s11665-021-05919-6.

[20] B. Mondal, T. Mukherjee, T. DebRoy, Crack free metal printing using physics informed machine learning, Acta Mater. 226 (2022) 117612. https://doi.org/10.1016/j.actamat.2021.117612.

Academic Vita

James Hanagan

Education

THE PENNSYLVANIA STATE UNIVERSITY | UNIVERSITY PARK, PA

- Bachelor of Science in Materials Science and Engineering (graduating May 2022)
- Schreyer Honors Scholar
- **Significant Coursework:** Materials Characterization, Mechanical Properties, Crystal Chemistry, Phase Relations, Computational Materials Science, MATLAB for engineers, Technical Communication, Ferrous and Non-ferrous Metallurgy, Metals Processing, Corrosion, Nondestructive Evaluation

Experience

RESEARCH INTERN | COLLINS AEROSPACE (MAY 2021 – AUGUST 2021)

- Characterized additively manufactured metal samples using optical microscopy (OM), scanning electron microscopy (SEM), energy-dispersive x-ray spectroscopy (EDS), and microhardness testing
- Repaired, operated, and wrote operating procedures for a polymer 3D printer
- Utilized Siemens NX to design and 3D print tools needed around the lab
- Assisted in optimizing development of AM processes by identifying, documenting, and recommending best practices to engineers involved

RESEARCH INTERN | CENTER FOR INNOVATIVE MATERIALS PROCESSING THROUGH DIRECT DIGITAL DEPOSITION (CIMP-3D) (MAY 2019 – PRESENT)

- Operating both metal and polymer AM machines
- Using SOLIDWORKS extensively to design and fabricate equipment for the lab
- Optimizing operation of AM machines through documentation and communication with operators
- Preparing documentation relevant to projects for sponsors and internal use
- Gaining a well-rounded knowledge of all aspects of additive manufacturing
- Performing research in process development for new materials

Skills

TECHNICAL SKILLS

- Uses CAD programs regularly, has experience with Autodesk Inventor, Onshape, SOLIDWORKS, and NX
- Knowledge of 3D modeling and simulation software nTop Platform
- Works extensively with 3D printers, both polymer and metal
- Experienced in Excel from calculus and materials science classes as well as documentation for lab work
- Well-versed in Microsoft Word for writing technical communication
- Familiar with materials characterization techniques such as OM, SEM, EDS and hardness testing

LEADERSHIP

- President – PSU Circle K Volunteer and Service Organization (March 2021 – March 2022)
- Service Project Chair – PSU Circle K Volunteer and Service Organization (March 2020 – March 2021)
- Secretary – Irvin Hall Special Living Option (SLO) (January 2019 – December 2019)
- Mentor – Centre County 4-H middle school FIRST robotics team (August 2018 – August 2019)
- Chair – Earth and Mineral Sciences (EMS) Student Council Relay for Life (October 2018 – April 2019)
- Representative – Irvin Hall SLO at EMS Student Council (August 2018 – December 2018)

Achievements & Awards

- Schreyer Honors Scholar (Fall 2019 – Spring 2022)
- Robert G. and Agnes M. Faber Scholarship for Materials Science and Engineering (Fall 2021 - Spring 2022)
- Matthew J. Wilson Honors Scholarship (Fall 2018 - Spring 2020, Fall 2021 - Spring 2022)
- Frederick C. Langenberg Scholarship in Materials Science and Engineering (Fall 2020 - Spring 2021)
- Richard M. Wardrop Honors Scholarship in Metals Science and Engineering (Fall 2020 - Spring 2021)
- Dean's List (Fall 2018 - Spring 2021)